Article

Shell buckling for programmable metafluids

Adel Djellouli[1,5], Bert Van Raemdonck[2,5], Yang Wang[1,5], Yi Yang[1], Anthony Caillaud[1], David Weitz[1], Shmuel Rubinstein[1,3], Benjamin Gorissen[1,4 ✉] & Katia Bertoldi[1 ✉]

The pursuit of materials with enhanced functionality has led to the emergence of metamaterials—artificially engineered materials whose properties are determined by their structure rather than composition. Traditionally, the building blocks of metamaterials are arranged in fixed positions within a lattice structure[1–19]. However, recent research has revealed the potential of mixing disconnected building blocks in a fluidic medium[20–27]. Inspired by these recent advances, here we show that by mixing highly deformable spherical capsules into an incompressible fluid, we can realize a 'metafluid' with programmable compressibility, optical behaviour and viscosity. First, we experimentally and numerically demonstrate that the buckling of the shells endows the fluid with a highly nonlinear behaviour. Subsequently, we harness this behaviour to develop smart robotic systems, highly tunable logic gates and optical elements with switchable characteristics. Finally, we demonstrate that the collapse of the shells upon buckling leads to a large increase in the suspension viscosity in the laminar regime. As such, the proposed metafluid provides a promising platform for enhancing the functionality of existing fluidic devices by expanding the capabilities of the fluid itself.

Unlike solid metamaterials, metafluids have the unique ability to flow and adapt to the shape of their container without the need for a precise arrangement of their constituent elements. Our goal is to realize a metafluid that not only has these remarkable attributes but also provides a platform for programmable compressibility, optical properties and rheology. To achieve this, we focus on a suspension comprising elastomeric, highly deformable spherical capsules filled with air within an incompressible fluid. We begin by considering centimetre-scale capsules that are fabricated out of silicone rubber (Zhermack Elite Double 32 with initial shear modulus $G = 0.35$ MPa) using 3D-printed moulds[28,29] (see Supplementary Fig. 1 and Supplementary Information for details). As shown in Fig. 1a, we place these capsules in a glass cylindrical container with volume V_{tot} and fill it completely with water. We then load the system by slowly introducing an additional volume ΔV of water via a syringe pump and measure the pressure inside the container with a differential pressure sensor (see also Supplementary Fig. 5).

We start by placing a single capsule with outer radius $R_o = 10$ mm and thickness $t = 2$ mm into a container with $V_{tot} = 300$ ml, leading to an initial capsule volume fraction of $\varphi = 4\pi R_o^3 N/(3V_{tot}) \approx 0.014$ ($N = 1$ denoting the number of capsules in the suspension). We record a pressure–volume curve that is very different from that of water, not only because the capsule makes the fluid more compressible (lowering the initial bulk modulus K_0 to 31 MPa) but also because it introduces a sudden pressure drop at the critical pressure $P = P_{cr}^{up} = 120$ kPa (Supplementary Fig. 1b and Supplementary Video 1). This drop is caused by the snapping of the elastomeric shell and leads to the formation of a dimple, which becomes more accentuated as ΔV is increased (inset in Fig. 1b). When unloading the suspension by decreasing ΔV, the dimple progressively reduces in size and the capsule snaps back to a spherical shape when the pressure passes the critical pressure $P = P_{cr}^{down} = 50$ kPa, leading to a hysteretic response.

To better understand the dependence of the metafluid characteristic on the properties of the capsules, we then consider a larger capsule with $R_o = 30$ mm and $t = 6$ mm in a container with $V_{tot} = 2,850$ ml, so that $t/R_o = 0.2$ remains unaltered and φ increases to 0.04. In this case, the system shows a lower initial bulk modulus ($K_0 = 18$ MPa), but still shows a pressure drop at $P_{cr}^{up} = 120$ kPa (red line in Fig. 1c), suggesting that K_0 and P_{cr}^{up} can be tuned independently by varying φ and t/R_o. Next, we investigate the effect of the number of capsules by placing $N = 27$ capsules with $R_o = 10$ mm and $t = 2$ mm in the same container with $V_{tot} = 2,850$ ml. As both φ and t/R_o remain the same (that is, $\varphi = 0.04$ and $t/R_o = 0.2$), the suspension shows the same initial bulk modulus (green line in Fig. 1c) and all capsules snap at $P \approx P_{cr}^{up}$ (snapshots in Fig. 1c and Supplementary Video 2). However, in this case, the large snapping-induced pressure drop observed for $N = 1$ is replaced by 27 small drops, where each drop corresponds to the collapse of a single capsule. These individual drops occur at roughly the same pressure such that a plateau emerges (see Supplementary Figs. 4–7 for additional experimental results).

The results in Fig. 1a–c are for a fluid containing centimetre-scale capsules, but most applications of fluids require the capability of flowing through small openings. Therefore, we take advantage of microcapillarity[30,31] to fabricate spherical capsules with $R_o \approx 250$ μm and $t \approx 65$ μm out of polydimethylsiloxane (PDMS; Fig. 1d and Supplementary Figs. 2 and 3). We characterize the pressure–volume curve of the resulting microcapsule suspension by placing it in a syringe with volume V_{tot} and slowly displacing the plunger to reduce the enclosed volume by ΔV, while keeping the tip closed and monitoring the pressure (see Supplementary Fig. 10 and Supplementary Information for more details). In Fig. 1e,f, we report the pressure–volume curves measured for a single microcapsule and for a suspension of many microcapsules with $\varphi = 0.3$, respectively (see also Supplementary Videos 1 and 2).

[1]J.A. Paulson School of Engineering and Applied Sciences, Harvard University, Cambridge, MA, USA. [2]Department of Mechanical Engineering, KU Leuven and Flanders Make, Heverlee, Belgium. [3]Present address: The Racah Institute of Physics, The Hebrew University, Jerusalem, Israel. [4]Present address: Department of Mechanical Engineering, KU Leuven and Flanders Make, Heverlee, Belgium. [5]These authors contributed equally: Adel Djellouli, Bert Van Raemdonck, Yang Wang. ✉e-mail: benjamin.gorissen@kuleuven.be; bertoldi@seas.harvard.edu
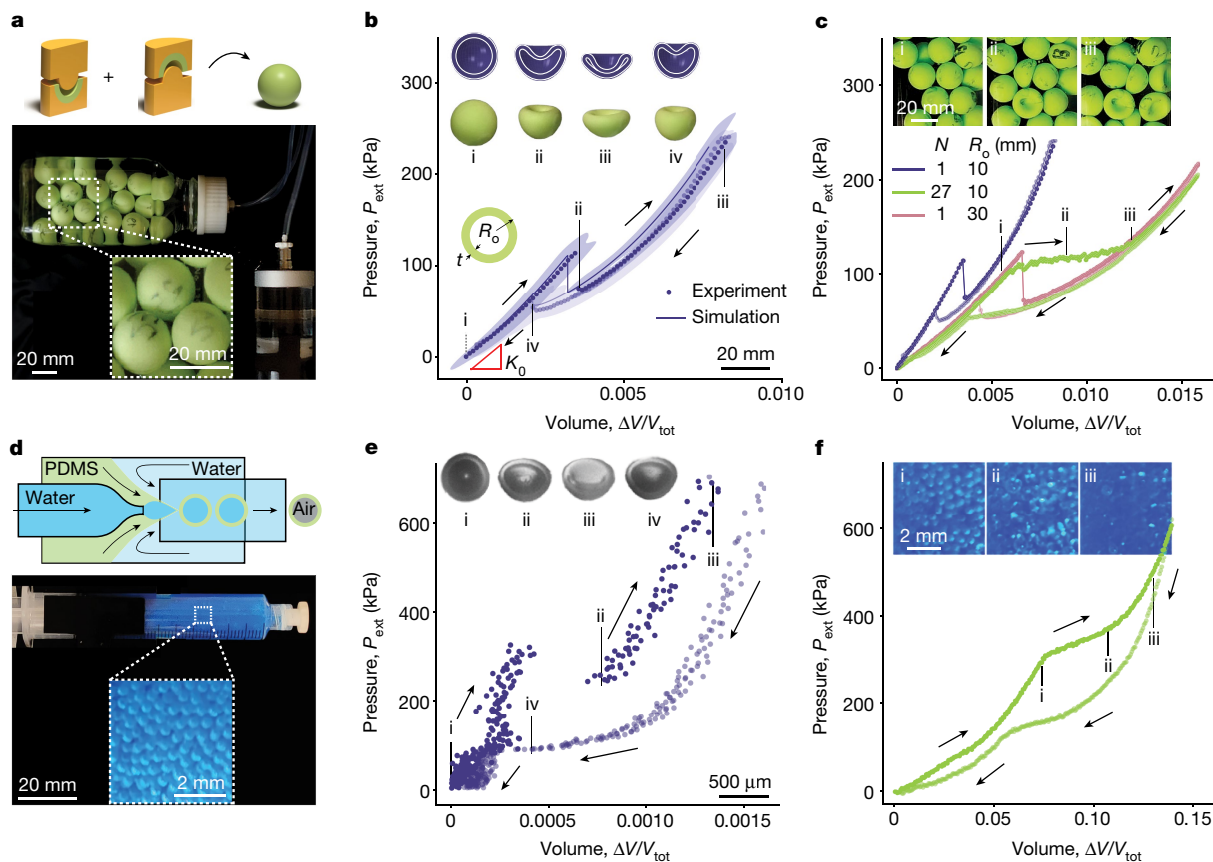
Fig. 1 | Metafluid comprising highly deformable capsules. a, Our centimetre-scale capsules are fabricated via a moulding approach and suspended in a fluid. The resulting metafluid is then pressurized. **b**, Pressure–volume curve of a single centimetre-scale capsule with $t = 2$ mm and $R_o = 10$ mm. Loading (dark purple) and unloading (light purple) curves are shown. The experimental data are depicted as average (dots) and standard deviation (shaded area) of five samples fabricated using the same mould and material. The solid line indicates finite-element results. Insets: experimental (bottom) and numerical (top) snapshots of the capsule. **c**, Experimental pressure–volume curves of metafluids comprising centimetre-scale capsules. Insets: snapshots of the metafluid at different level of compression. **d**, Our micrometre-scale capsules are fabricated from double emulsions using a co-axial flow focusing glass microfluidic device. **e**, Experimental pressure–volume curve of a single micrometre-scale capsule with $t \approx 65$ μm and $R_o = 250$ μm. **f**, Experimental pressure–volume curves of metafluids comprising micrometre-scale capsules with a volume fraction $\varphi \approx 0.3$ suspended in silicone oil. Insets: snapshots of the metafluid at different levels of compression.

The curves show qualitatively similar nonlinear behaviours to their centimetre-scale counterparts, confirming that the response of our metafluids is independent of scale. Nevertheless, it is important to highlight that the metafluid incorporating microscale capsules does not show a clear plateau in the pressure–volume curve. This deviation can be attributed to geometric imperfections introduced during the fabrication process, resulting in polydispersity and a wide range of buckling pressures P_{cr}^{up}.

Modelling

To systematically explore the effect of the capsules on the response of the metafluid, we conduct finite-element analyses using the commercial package ABAQUS 2020 Standard. In our simulations, we assume the deformation to be axisymmetric and use an incompressible Neo–Hookean material model with initial shear modulus G to capture the response of the elastomeric material (see Supplementary Figs. 15–25, Supplementary Tables 1 and 2, and Supplementary Information for additional details). We first conduct implicit dynamic simulations to calculate the difference between the external and internal pressure of the shells, ΔP_{shell}, while slowly decreasing and then increasing the volume of their internal cavity by ΔV (purple line in Fig. 2a). Then we use the ideal gas law to obtain the pressure of the gas enclosed in the shell cavity, P_{int}, as a function of ΔV (cyan line in Fig. 2a). Finally, we take advantage of the shell incompressibility to calculate the pressure on the external surface of the capsule, P_{ext}, as

$$P_{ext} = \Delta P_{shell}(\Delta V) + P_{int}(\Delta V). \tag{1}$$

The results reported in Fig. 2a indicate that, since P_{int} increases monotonically with ΔV, the nonlinear response of the metafluid stems from ΔP_{shell}. We also note that P_{ext} does not scale with G, as P_{int} is independent of the shell material (Supplementary Fig. 19). Further, we point out that if the pressure is controlled during the tests, snapping triggers a jump in volume at P_{cr} (dotted lines in Fig. 2a). Finally, we test the relevance of our model by comparing its predictions with the experimental results reported in Fig. 1b as well as to the experimentally measured P_{cr}^{up} and P_{cr}^{down} for a variety of centimetre-scale capsules (Fig. 2b) and find excellent agreement.

Having established a numerical model that accurately captures the response of the individual capsules, we use it to predict the response of suspensions comprising many capsules. Towards this end, we assume that the capsules are suspended in an incompressible fluid and that the pressure is uniform throughout this medium (thereby neglecting the effects of gravity and viscosity). Under these assumptions, the external pressure is the same for all N capsules

$$P_{ext}^{(1)}(\Delta V^{(1)}) = P_{ext}^{(2)}(\Delta V^{(2)}) = \ldots = P_{ext}^{(N)}(\Delta V^{(N)}), \tag{2}$$
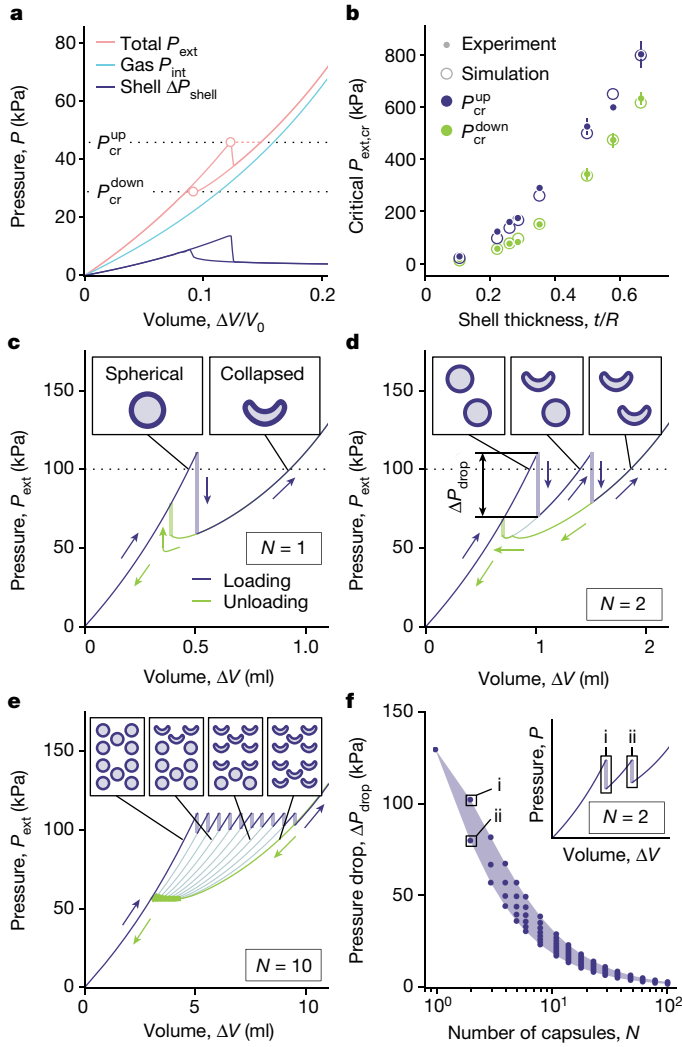
Fig. 2 | Modelling metafluids. a, Numerically predicted pressure–volume curve for a spherical shell with $t/R = 0.22$ and $G = 60$ kPa (cyan line), the gas contained in its internal cavity (blue line) and the resulting capsule (pink line) under volume control. If the capsule is loaded under pressure control, the instabilities are triggered at the circular markers and follow the dotted lines. **b**, Critical pressures as a function of shell thickness for capsules with $G = 350$ kPa. Both numerical (hollow circular markers) and experimental data (dots) are shown. Vertical lines on the experimental data points indicate the standard deviation between shells manufactured with the same mould. **c–e**, Numerical pressure–volume curve for a metafluid containing $N = 1$ (**c**), $N = 2$ (**d**) and $N = 10$ (**e**) capsules with $R_o = 10$ mm, $t = 2$ mm and $G = 350$ kPa. Insets: the state of the capsules for different ΔV at $P_{ext} = 100$ kPa. **f**, Evolution of the pressure drop triggered by buckling, ΔP_{drop}, as a function of the number of capsules in a metafluid, N. Inset: the pressure–volume curve for a metafluid comprising $N = 2$ capsules that produces the data points labelled i and ii.

where $\Delta V^{(i)}$ denotes the change in volume of the ith capsule in the pressurized state, which is subjected to the constraint

$$\Delta V = \sum_{i=1}^{N} \Delta V^{(i)}. \qquad (3)$$

It is noted that equations (2) and (3) together with the $P_{ext}^{(i)} – \Delta V^{(i)}$ curves extracted from the finite-element simulations are analogous to the relations between force and displacement for chains of bistable elements with trilinear characteristics[32,33], with the only difference being that for the capsules the portion of the pressure–volume curve immediately after snapping is inherently unstable.

Operationally, we determine all of the equilibrium configurations of a metafluid comprising N capsules by first finding all stable $\Delta V^{(i)}$ that result in a predefined set of pressure values for each capsule separately (Fig. 2c). Then for each value of pressure, we construct the possible equilibrium states of the metafluid by making all possible combinations of those volumes. As shown in Fig. 2d,e, for a suspension comprising N identical capsules, this process generates a pressure–volume characteristic with $N + 1$ unique equilibrium branches. When the suspension is loaded by slowly introducing a volume ΔV of incompressible fluid, the first branch is initially followed until the critical buckling pressure of the capsules, P_{cr}^{up}, is reached. At that point, one capsule snaps and the pressure drops (at constant ΔV) until it reaches the next branch. This process then repeats until all N capsules are collapsed, leading to a sawtooth pattern with N peaks at P_{cr}^{up}. As observed in our experiments, we find that the magnitude of the pressure drops that follow the buckling events, ΔP_{drop}, decreases with N (Fig. 2f). This decrease is due to the fact that in a suspension with N capsules, the sudden reduction in volume experienced by one capsule upon snapping can be compensated by a slight expansion of the remaining $N - 1$ capsules (see Supplementary Information for more details). Therefore, for large N, ΔP_{drop} tends to zero and each capsule can be considered to experience pressure control conditions even though the total volume of the metafluid is controlled.

Harnessing the nonlinear metafluid behaviour

Guided by our understanding of the metafluid response, we then harness its highly nonlinear behaviour for functionality. First, we exploit the snapping-induced pressure plateau to realize a gripper that can grasp objects of very different size and compressive strength when actuated with the same input. More specifically, we consider a two-jaw parallel gripper actuated by pressurized fluid (Fig. 3a, top left) and focus on three distinct objects: a glass bottle of 60 mm in diameter and 160 g in weight, an egg of about 25 mm in diameter and about 16 g in weight, and a blueberry of about 10 mm in diameter and about 0.5 g in weight. For a successful grasp, the supplied volume, ΔV, must be large enough for the actuated jaw to reach the object and hold its weight, but not so large as to generate an excessive force that crushes it (Fig. 3a, top right). In particular, for the considered bottle, egg and blueberry, the supplied volume required to reach them and the pressures needed to hold them and crush them are measured as $\Delta V_{reach} \approx 1.1$ ml, $\Delta V_{reach} \approx 3.9$ ml and $\Delta V_{reach} \approx 5.1$ ml, $P_{hold} \approx 110$ kPa, $P_{hold} \approx 12$ kPa and $P_{hold} \approx 1$ kPa, and $P_{crush} \approx 700$ kPa, $P_{crush} \approx 105$ kPa and $P_{crush} \approx 55$ kPa, respectively. When using water or air as fluid to actuate the jaw, no ΔV can be identified that allows us to successfully grasp all three objects (see Supplementary Fig. 8, Supplementary Video 3 and Supplementary Information for more details). By contrast, when using our metafluid with $K_0 = 2$ MPa and two plateaus at 45 kPa and 120 kPa (realized by filling a container with $V_{tot} = 100$ ml with water and six capsules with $t = 2$ mm and $R_o = 10$ mm, three made out of rubber with $G = 60$ kPa and three made out of rubber with $G = 350$ kPa), we can successfully grasp all three objects by injecting $\Delta V = 6.7$ ml (Fig. 3a, bottom, and Supplementary Video 3).

Although in Fig. 3a we use centimetre-scale capsules enclosed in a separate container to regulate the pressure of the fluid, such an independent pressure reservoir is unnecessary when utilizing our microsuspension, as it can be directly placed in the functional components. To demonstrate this, we use the microsuspension of Fig. 1f to directly pressurize a flexible latex tube (shear modulus $G \approx 1$ MPa) with outer diameter of 5.1 mm, thickness of 1.9 mm and length of 48 mm. Such a tube undergoes a ballooning instability at a pressure $P_{cr}^{tube} \approx 400$ kPa, which upon inflation with glycerol is reached for $\Delta V \approx 0.53$ ml (red line in Fig. 3b and Supplementary Video 4). The compliance and pressure plateau of the microsuspension offset the ballooning instability to $\Delta V \approx 0.94$ ml (green line in Fig. 3b and Supplementary Video 4), showing that the nonlinear behaviour of the capsules also provides an
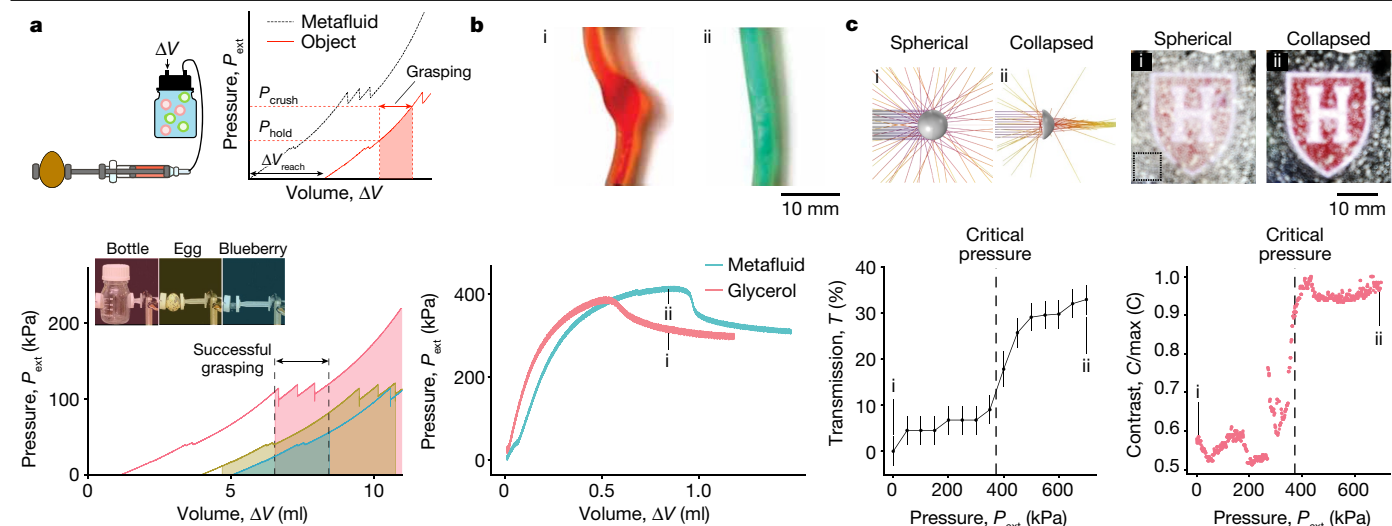
Fig. 3 | Programming metafluids for functionality. a, A two-jaw parallel gripper actuated by our metafluid can grasp a bottle, an egg and a blueberry upon application of the same input $\Delta V = 6.7$ ml (dashed lines in bottom panel). Top left, the experimental setup. Top right, having determined ΔV_{reach}, P_{hold} and P_{crush}, the volume ΔV to be supplied to the system to successfully grasp an object can be easily identified by shifting the pressure–volume curve of the considered fluid (black dashed line) horizontally by ΔV_{reach} for that object. We then identify the volumes ΔV for which $P_{hold} \leq P_{ext} \leq P_{crush}$ (see regions highlighted in red, yellow and blue in the plot). Bottom, the range of ΔV that enables successful grasping of the bottle, egg and blueberry is between the two vertical dashed lines. **b**, Inflation of a flexible tube with our microsuspension. The ballooning instability is delayed to $\Delta V \approx 0.94$ ml. Top, snapshots of the tube upon inflation with glycerol (left) and the metafluid (right) for $\Delta V = 0.9$ ml. Bottom, pressure–volume curves recorded upon inflation with glycerol and the metafluid. **c**, Top left: tunable optics, ray-tracing simulation for spherical and collapsed capsules. Bottom left: relative transmittance T as function of pressure P_{ext}. The black dashed line represents P_{cr}^{up} of the metafluid. Top right: a Harvard logo displayed below the metafluid is clearer for $P_{ext} > P_{cr}^{up}$. Bottom right: this is confirmed by the evolution of the contrast C as function of the pressure P_{ext}. The contrast was measured in the region outlined by the dashed square on snapshot (i).

opportunity to tune the interactions of the metafluid with surrounding flexible structures.

Apart from the nonlinear pressure–volume curve, the substantial alterations in the shape of the capsule induced by instability also present opportunities for functionality. Inspired by the configuration-dependent interactions with light observed for droplets[34], we investigate the effect of the pronounced dimple caused by buckling on the optical properties of the metafluid. To this end, we conduct simulations in COMSOL using a ray-tracing algorithm (see Supplementary Information for details). As shown in Fig. 3c, top left, the simulations show that spherical and collapsed capsules show distinct scattering behaviours (Supplementary Figs. 26 and 27). When we then measure the power of the transmitted light through a microsuspension with $\varphi \approx 0.4$ and $P_{cr}^{up} \approx 380$ kPa, we find that the transmittance T suddenly increases from $T \approx 8\%$ to $T \approx 30\%$ at $P_{ext} \approx P_{cr}^{up}$ (Fig. 3c, bottom left, and Supplementary Fig. 11). This increase can be attributed to a combination of the lensing effect and the reduction in the coverage area of the capsules in the collapsed state (see Supplementary Figs. 26–28 and Supplementary Information for details). Such a large change in transmittance makes a Harvard logo, positioned beneath the metafluid, much clearer for $P_{ext} > P_{cr}^{up}$ (Fig. 3c, top right, and Supplementary Video 5), as demonstrated by the sharp increase in contrast when the capsules snap (Fig. 3c, bottom right).

The buckling-induced shape change of the capsules also modifies the way in which the metafluid flows. To demonstrate this point, we consider a microsuspension with $\varphi \approx 0.3$ and $P_{cr}^{up} = 300$ kPa and investigate its flow in an elliptical channel with major axis $a_{ch} = 3$ mm and minor axis $b_{ch} = 750$ µm. We fix the difference of pressure between the inlet and outlet at $\Delta P = P_{in} - P_{out} = 50$ kPa and conduct experiments for $P_{in} \in [50, 450]$ kPa (Fig. 4a, Supplementary Figs. 12 and 13, and Supplementary Video 6). For each experiment, we monitor the position of the front once the flow is fully developed and then calculate its average velocity, $\bar{v}_{front}$. As expected, we find that for $50 \leq P_{in} \leq 250$ kPa, the velocity of the front increases with the pressure at the inlet (Fig. 4b). For

this range of P_{in}, the capsules retain their spherical shape and isotropically shrink as the pressure increases, leading to a decreasing effective capsule volume fraction and, in turn, to a faster flow[35–37]. However, when the pressure is high enough to snap the capsules, $\bar{v}_{front}$ largely decreases. The unexpected drop in flow velocity can be explained by the formation of a dimple upon buckling, which causes the capsules to adopt a concave shape. This concave shape significantly modifies the interactions between particles, resulting in the formation of clusters and aggregates that ultimately slow down the flow[38] (Supplementary Video 6). Importantly, this transition is reversible and repeatable as the shape change of the capsules is driven by an elastic instability (Supplementary Video 6). The results in Fig. 4b suggest that the effective viscosity of the metafluids is higher when the capsules are collapsed. Nonetheless, it is important to note that in these experiments the metafluid is sheared at a rate $\dot{\gamma} \approx 1$ s^{-1}. To investigate how the effective viscosity of the metafluid is affected by the shear rate, we characterize its rheology using a parallel plate rheometer (see Supplementary Fig. 14 and Supplementary Information for details). The results reported in Fig. 4c indicate that the collapse of the particles have a profound effect on its rheology. In the presence of spherical capsules, the metafluid behaves as a Newtonian fluid with effective viscosity $\eta \approx 2.2\eta_0$ (η_0 denoting the viscosity of the solvent). However, when the capsules are collapsed, the suspension transforms into a non-Newtonian shear-thinning fluid. In line with the results in Fig. 4a,b, the metafluid containing collapsed capsules shows high effective viscosity at low shear rates. Such behaviour is ascribed to the formation of clusters by the collapsed particles, as previously reported for blood containing sickle-shaped red blood cells[39]. As the shear rate increases, we observe an initial rapid decrease in effective viscosity, which we attribute to the gradual disruption of the clusters. Eventually, at $\dot{\gamma} \approx 10$ s^{-1} the effective viscosity approaches a plateau at $1.3\eta_0$. This plateau can be attributed to the breakdown of particle clusters at such high strain rates. Finally, we note that at high shear rates, the effective viscosity of the metafluid containing collapsed particles is lower than that of the metafluid containing
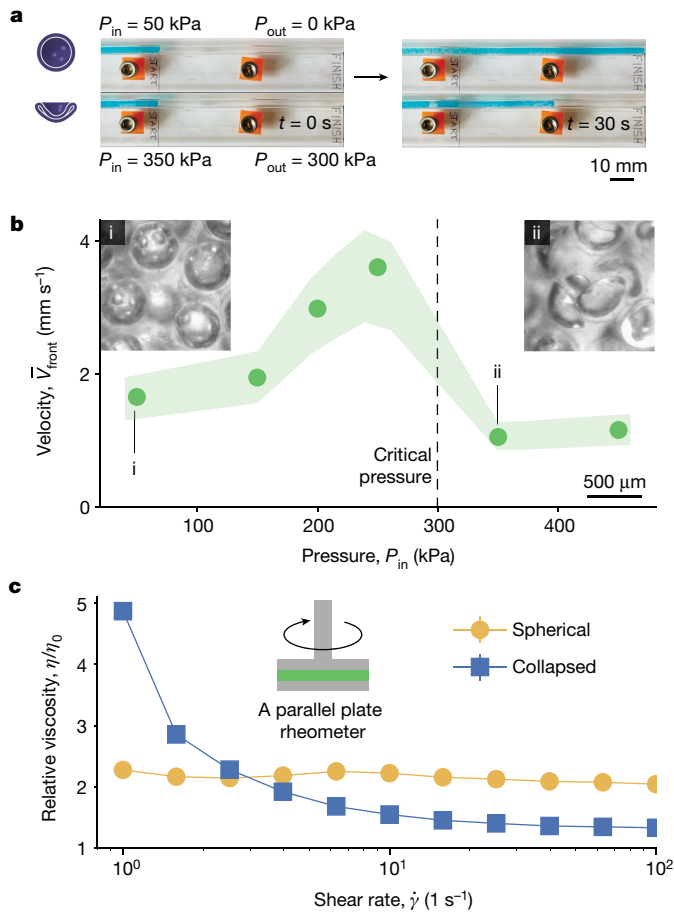
Fig. 4 | Harnessing nonlinearity for tunable rheology. a, Snapshots of the metafluid with $P_{cr}^{up} \approx 300$ kPa flowing in a channel under constant difference of pressure $\Delta P = P_{in} - P_{out} = 50$ kPa at $t = 0$ (left) and $t = 30$ s. Top: $P_{in} = 50$ kPa so that the capsules are spherical. Bottom: $P_{in} = 350$ kPa so that the capsules are collapsed. **b**, Average front velocity as function of P_{in} for $\Delta P = 50$ kPa. The experimental data are depicted as average (markers) and standard deviation (shaded area). Snapshots show the flowing microsuspension for $P_{in} = 50$ kPa and $P_{in} = 350$ kPa. **c**, Flow curves for a metafluid containing spherical (yellow markers) and collapsed (blue markers) capsules.

spherical ones, probably because of the decrease in particle volume fraction caused by buckling. Altogether, these experiments highlight that the metafluid shows rich rheology that can be tuned by controlling shape of the capsules through the level of the applied pressure.

Conclusion

In summary, we have successfully demonstrated the potential of utilizing reversible buckling of elastomeric shells to create a novel class of metafluids. These metafluids show programmable compressibility, switchable optical properties and adjustable viscosity. The versatility of these metafluids opens numerous opportunities for functionality, as demonstrated by the development of adaptable grippers and reconfigurable logic gates (see Supplementary Fig. 9 and Supplementary Information for details). Moreover, we anticipate that the programmability of these metafluids will have significant implications for acoustic and thermodynamic properties, enabling the enhancement of thermodynamic cycles and customizable sound propagation. All these applications would benefit from an inverse design platform capable of identifying shell mixtures that yield desired responses. For example, inversely designed metafluids with complex nonlinear behaviour could be used to modify the functionality of soft actuators by simply changing the actuating fluid instead of redesigning the actuator itself for the new task. Furthermore, they could pave the way towards smart hydraulic shock absorbers with dissipation tailored to the profile of the shock. Finally, while this study primarily focused on situations involving slow loading, dynamic pressure drops across the metafluid could open opportunities for a spatial avalanche of snapping events and interesting wave propagation.

Online content

Any methods, additional references, Nature Portfolio reporting summaries, source data, extended data, supplementary information, acknowledgements, peer review information; details of author contributions and competing interests; and statements of data and code availability are available at https://doi.org/10.1038/s41586-024-07163-z.

1. Engheta, N. & Ziolkowski, R. W. *Metamaterials: Physics and Engineering Explorations* (Wiley, 2006).
2. Craster, R. V. & Guenneau, S. *Acoustic Metamaterials: Negative Refraction, Imaging, Lensing and Cloaking* Vol. 166 (Springer Science & Business Media, 2012).
3. Deymier, P. A. *Acoustic Metamaterials and Phononic Crystals* Vol. 173 (Springer Science & Business Media, 2013).
4. Maldovan, M. Narrow low-frequency spectrum and heat management by thermocrystals. *Phys. Rev. Lett.* **110**, 025902 (2013).
5. Bertoldi, K., Vitelli, V., Christensen, J. & Van Hecke, M. L. Flexible mechanical metamaterials. *Nat. Rev. Mater.* **2**, 17066 (2017).
6. Kadic, M., Bückmann, T., Schittny, R. & Wegener, M. Metamaterials beyond electromagnetism. *Rep. Prog. Phys.* **76**, 126501 (2013). ISSN 0034-4885.
7. Christensen, J., Kadic, M., Kraft, O. & Wegener, M. Vibrant times for mechanical metamaterials (book review). *MRS Commun.* **5**, 453–462 (2015).
8. Lee, G. et al. Piezoelectric energy harvesting using mechanical metamaterials and phononic crystals. *Commun. Phys.* **5**, 94 (2022).
9. Xu, X. et al. Multifunctional metamaterials for energy harvesting and vibration control. *Adv. Funct. Mater.* **32**, 2107896 (2022).
10. Hu, G., Tang, L., Liang, J., Lan, C. & Das, R. Acoustic-elastic metamaterials and phononic crystals for energy harvesting: a review. *Smart Mater. Struct.* **30**, 085025 (2021).
11. Chen, Z., Guo, B., Yang, Y. & Cheng, C. Metamaterials-based enhanced energy harvesting: a review. *Physica B* **438**, 1–8 (2014).
12. Fowler, C., Silva, S., Thapa, G. & Zhou, J. High efficiency ambient RF energy harvesting by a metamaterial perfect absorber. *Opt. Mater. Express* **12**, 1242–1250 (2022).
13. Ramahi, O. M., Almoneef, T. S., AlShareef, M. & Boybay, M. S. Metamaterial particles for electromagnetic energy harvesting. *Appl. Phys. Lett.* **101**, 173903 (2012).
14. Lin, Keng-Te., Lin, H., Yang, T. & Jia, B. Structured graphene metamaterial selective absorbers for high efficiency and omnidirectional solar thermal energy conversion. *Nat. Commun.* **11**, 1389 (2020).
15. Cortés, E. et al. Optical metasurfaces for energy conversion. *Chem. Rev.* **122**, 15082–15176 (2022).
16. Patel, S. K., Surve, J., Katkar, V. & Parmar, J. Optimization of metamaterial-based solar energy absorber for enhancing solar thermal energy conversion using artificial intelligence. *Adva. Theory Simul.* **5**, 2200139 (2022).
17. Chen, T., Li, S. & Sun, H. Metamaterials application in sensing. *Sensors* **12**, 2742–2765 (2012).
18. Molerón, M. & Daraio, C. Acoustic metamaterial for subwavelength edge detection. *Nat. Commun.* **6**, 8037 (2015).
19. Fan, W., Yan, B., Wang, Z. & Wu, L. Three-dimensional all-dielectric metamaterial solid immersion lens for subwavelength imaging at visible frequencies. *Sci. Adv.* **2**, e1600901 (2016).
20. Urzhumov, Y. A. et al. Plasmonic nanoclusters: a path towards negative-index metafluids. *Opt. Express* **15**, 14129–14145 (2007).
21. Sheikholeslami, S. N., Alaeian, H., Koh, Ai. Leen. & Dionne, J. A. A metafluid exhibiting strong optical magnetism. *Nano Lett.* **13**, 4137–4141 (2013).
22. Yang, J. et al. Broadband absorbing exciton-plasmon metafluids with narrow transparency windows. *Nano Lett.* **16**, 1472–1477 (2016).
23. Hinamoto, T., Hotta, S., Sugimoto, H. & Fujii, M. Colloidal solutions of silicon nanospheres toward all-dielectric optical metafluids. *Nano Lett.* **20**, 7737–7743 (2020).
24. Kim, K., Yoo, SeokJae, Huh, Ji-Hyeok, Park, Q.-Han & Lee, S. Limitations and opportunities for optical metafluids to achieve an unnatural refractive index. *ACS Photon.* **4**, 2298–2311 (2017).
25. Cho, Y. et al. Using highly uniform and smooth selenium colloids as low-loss magnetodielectric building blocks of optical metafluids. *Opt. Express* **25**, 13822–13833 (2017).
26. Brunet, T. et al. Soft 3D acoustic metamaterial with negative index. *Nat. Mater.* **14**, 384–388 (2015).
27. Peretz, O., Ben Abu, E., Zigelman, A., Givli, S. & Gat, A. D. A metafluid with multistable density and internal energy states. *Nat. Commun.* **13**, 1810 (2022).
28. Djellouli, A., Marmottant, P., Djeridi, H., Quilliet, C. & Coupier, G. Buckling instability causes inertial thrust for spherical swimmers at all scales. *Phys. Rev. Lett.* **119**, 224501 (2017).
29. Jambon-Puillet, E., Jones, T. J. & Brun, P.-T. Deformation and bursting of elastic capsules impacting a rigid wall. *Nat. Phys.* **16**, 585–589 (2020).
30. Utada, A. S. Monodisperse double emulsions generated from a microcapillary device. *Science* **308**, 537–541 (2005).

Article

31. Chen, Q. Robust fabrication of ultra-soft tunable PDMS microcapsules as a biomimetic model for red blood cells. *Soft Matter* **19**, 5249–5261 (2023).
32. Puglisi, G. & Truskinovsky, L. Mechanics of a discrete chain with bi-stable elements. *J. Mech. Phys. Solids* **48**, 1–27 (2000).
33. Benichou, I. & Givli, S. Structures undergoing discrete phase transformation. *J. Mech. Phys. Solids* **61**, 94–113 (2013).
34. Nagelberg, S. et al. Reconfigurable and responsive droplet-based compound micro-lenses. *Nat. Commun.* **8**, 14673 (2017).
35. Guazzelli, É., Morris, J. F. & Pic, S. *A Physical Introduction to Suspension Dynamics* Cambridge Texts in Applied Mathematics (Cambridge Univ. Press, 2011).
36. Shewan, H. M. & Stokes, J. R. Viscosity of soft spherical micro-hydrogel suspensions. *J. Colloid Interface Sci.* **442**, 75–81 (2015).
37. Shewan, H. M. & Stokes, J. R. Analytically predicting the viscosity of hard sphere suspensions from the particle size distribution. *J. Nonnewton. Fluid Mech.* **222**, 72–81 (2015).
38. Dressaire, E. & Sauret, A. Clogging of microfluidic systems. *Soft Matter* **13**, 37–48 (2017).
39. Chien, S., Usami, S. & Bertles, J. F. Abnormal rheology of oxygenated blood in sickle cell anemia. *J. Clin. Invest.* **49**, 623–634 (1970).

Methods

The details of the fabrication methods are summarized in Supplementary Information section 1. The experimental procedure for all the experiments conducted for this study are described in Supplementary Information section 2. Finally, information about the modelling is provided in Supplementary Information section 3.

Data availability

The data that support the findings of this study are openly available in GitHub at https://github.com/BertVanRaemdonck/Buckling-Capsule-Metafluids.

Author contributions A.D., B.G., B.V.R. and K.B. proposed and developed the research idea. A.D., Y.Y. and A.C. designed and fabricated the centimetre-scale capsules. Y.W. fabricated and characterized the micrometre-scale capsules. A.D. designed and conducted the experiments and optical simulations. B.V.R. conducted the numerical calculations. A.D., B.V.R. and K.B. wrote the paper. K.B., B.G., S.R. and D.W. supervised the research.

Supplementary information

Shell buckling for programmable metafluids

Supplementary Materials

Shell Buckling for Programmable Metafluids

Adel Djellouli, Bert Van Raemdonck, Yang Wang, Yi Yang, Anthony Caillaud, David Weitz, Shmuel Rubinstein, Benjamin Gorissen, Katia Bertoldi

E-mail: bertoldi@seas.harvard.edu

This PDF file includes:

Supporting Information Text

S1. Fabrication

This section describes the fabrication of the elastomeric capsules at both the centimeter- and micrometer-scale.

S1.1. Fabrication of centimeter-scale capsules.

The centimeter-scale capsules used in this study are made of nearly incompressible polyvinylsiloxane (PVS) elastomers. We use Elite Double 32 from Zhermack (with green color and initial shear modulus $\mu = 0.35\,\mathrm{MPa}$). The Zhermack polyvinylsiloxane elastomer is generated by mixing two parts of uncured liquid polymers. As the two parts are mixed, the liquid will polymerize into a solid phase. The shell consists of two halves that are cast using a two-part mold, which is designed using NX 12 (Siemens) and 3D printed with foamlab SLA 3D printer. Both halves are molded separately and combined afterward to form a full spherical shell that encloses compressible air. The following step-by-step process is followed (see Fig S1):

- **Step 1:** we 3d print the molds, which comprise a convex part (light brown colored) and concave one (ivory colored).

- **Step 2:** we fill the concave part with uncured polyvinylsiloxane (PVS) elastomer mixture.

- **Step 3:** we close the molds with pressure clamps to ensure accurate layer thickness and place the samples at room temperature (25 Celsius) for 20 minutes.

- **Step 4:** we remove each cured semi-spherical shell from the mold and carefully bond two semi-spherical shells into one single capsule with uncured PVS elastomer.

- **Step 5:** we place every single capsule in two concave molds at room temperature for another 20 minutes for curing.
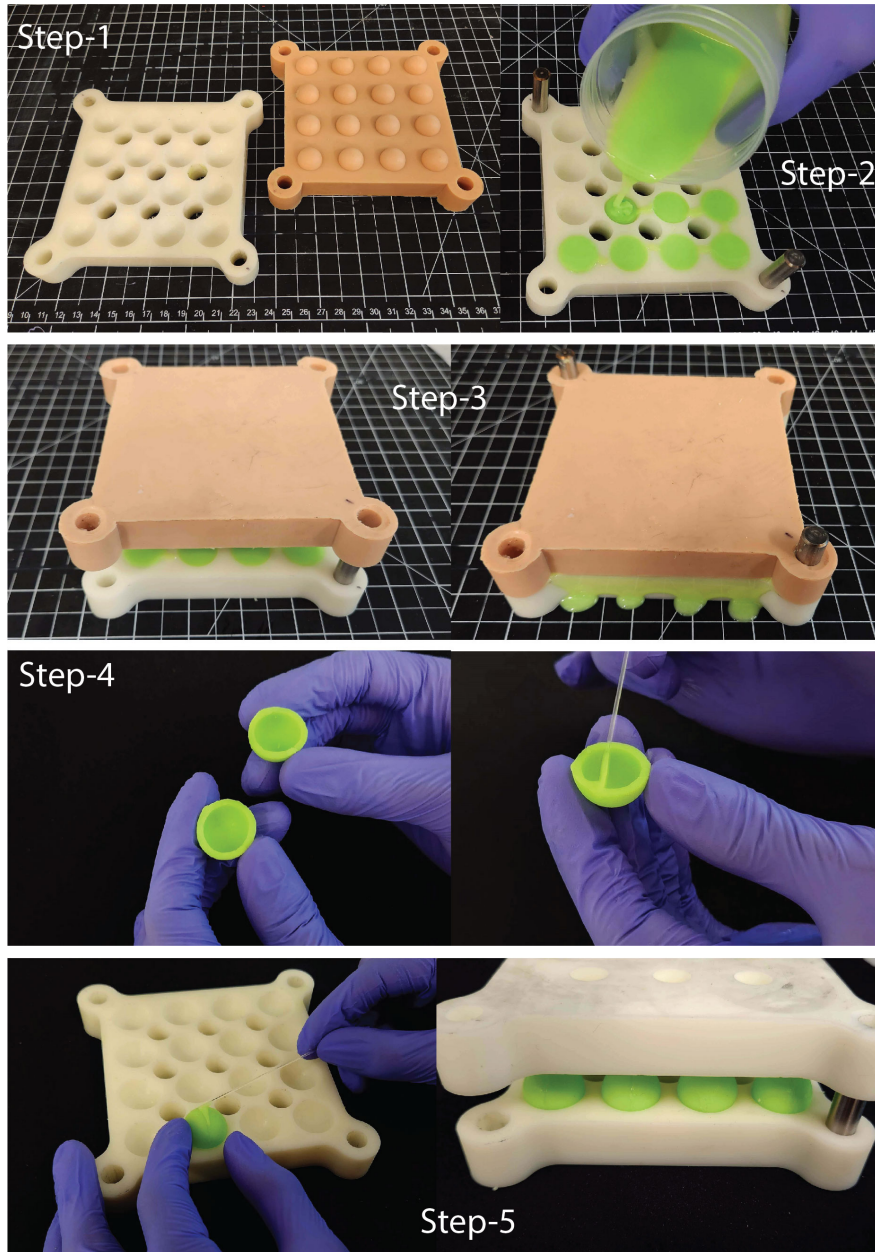
Fig. S1. Fabrication of centimeter-scale capsules. Snapshots of the 5 steps required to fabricate our centimeter-scale capsules.
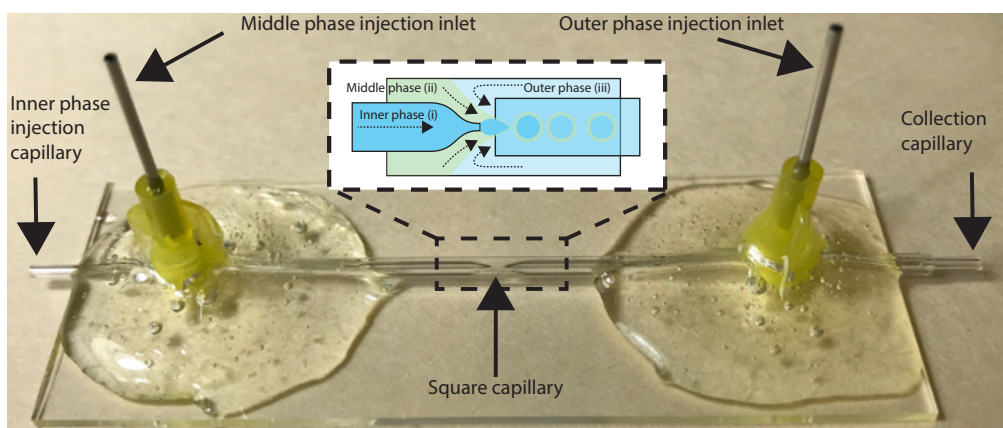
Fig. S2. Picture of the glass capillary device used in this study.

S1.2. Fabrication of micrometer-scale capsules.

The microcapsules considered in this study are produced from double emulsions using a co-axial flow focusing glass microfluidic device (1). More specifically, we used the capillary device shown in Fig. S2 that was assembled on a glass slide and comprises:

- An injection capillary made out of a glass tube with inner and outer diameter 0.2 and 1.0 mm, respectively (Cat. No. 1B100-6; World Precision Instruments, Inc.).

- A collection capillary made out of a glass tube with inner and outer diameter of 0.58 and 1.00 mm, respectively (Cat. No. 1B100-6; World Precision Instruments, Inc.).

- A square capillary made out of glass with inner and outer edges of 1.05 mm and 1.5 mm, respectively (Cat. No. 810-9917; AIT Glass Inc.). Note that the injection and collection capillaries are connected to this square capillary from opposite directions.

- A middle phase injection inlet which consists of a 20 gauge blunt tip dispensing needle.

- An outer phase injection inlet which consists of a 20 gauge blunt tip dispensing needle.

The tips of all capillaries were polished with sand paper to ensure smoothness. Further, the collection capillary was dipped inside 2-[Methoxy(Polyethylenoxy) propyl] trimethoxy silane) to make its inner surface hydrophilic. This capillary device was used to generate double emulsion droplets from the following phases

- Inner phase: polyvinyl alcohol (PVA) solution with 1% concentration;

- Middle phase: polydimethylsiloxane (PDMS- SYLGARD® 182) with a ratio between the base and the cure agent of 5 to 1 for the middle phase;

- Outer phase: polyvinyl alcohol (PVA) solution with 5% concentration.

To fabricate our microcapsules the following step-by-step process was followed (see Fig. S3)

- **Step 1:** double emulsion droplets were generated using the glass capillary devices shown in Fig. S2. The three phases were injected using syringe pumps (Harvard Apparatus, USA) connected to the injection capillaries through polyethylene tubes (BB31695-PE/4, Scientific37 Commodities Inc.) and the double emulsion droplets were collected in glass vials. Note that after collection the PVA concentration of the outer phase was decreased to 1% to balance osmotic pressure.

- **Step 2:** to minimize eccentricity between the inner and middle phases (which lead to capsule with non-unifrom thickness), all droplets were rotated in an oven supplied with a rotator (Hybridization Ovens, VWR) at 50 rpm and room temperature for two days.

- **Step 3:** all droplets were heated at 65 C for 8 hours to cure the PDMS (while rotating in the oven described in Step 2). Afterwards, the temperature was lowered to room temperature and the droplets sediment within 1 minute to the bottom of the vial. At this point, we removed the supernatant.

- **Step 4:** The capsules were placed in a freezer at -80°C for 24 hours.

- **Step 5:** The frozen capsules were placed in a freeze dryer (FreeZone® Triad® Benchtop Freeze Dryer) for at least 48 hours, under a 100 mtorr vacuum. This allowed the frozen inner core of the capsules to sublimate.

- **Step 6:** the freeze-dried capsules were flushed by deionized water to eliminate the PVA polymer left on their outer surface.

Note that to fabricate the PDMS microcapsules with outer radius of $R_o \approx 250\,\mu m$ considered in this study the flow rates of inner, middle and outer phases were kept at 1000, 1000 and 30000 $\mu L/h$. Differently, for the microcapsules with the outer radius of $R_o \approx 35\mu m$ that we used for the rheology experiments, the flow rates of inner, middle and outer phases were kept at 240, 240 and 10000 $\mu L/h$.
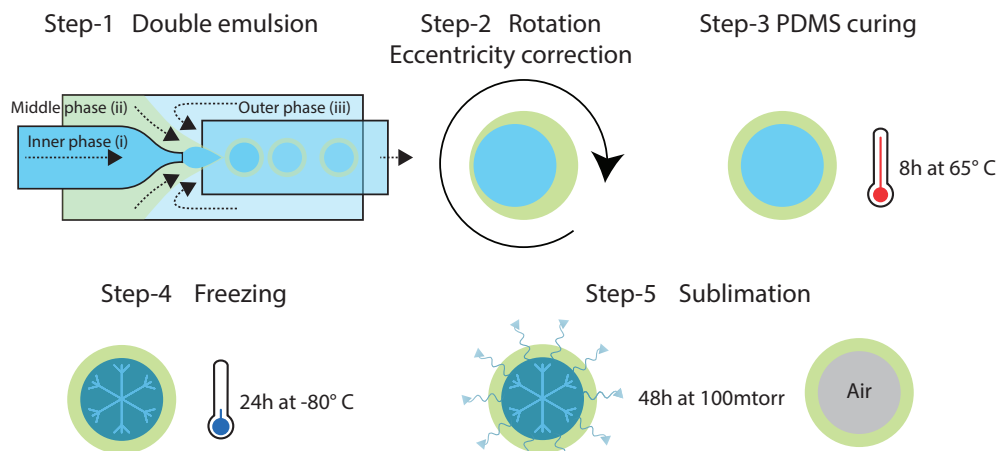
Fig. S3. Fabrication of micrometer-scale capsules. Schematics of the 5 steps required to fabricate our micrometer-scale capsules.

S2. Experiments

In this section we describe the procedure used for all the tests conducted with the metafluid with centimeter- and micrometer-scale capsules.

S2.1. Metafluid with centimeter-scale capsules.

Pressure-volume curve.   To characterize the pressure-volume characteristics of our metafluid with centimeter-scale capsules, we place it in a glass container. As shown in Fig. S5, we load the system by introducing a volume ΔV of water at a flow rate of 2.5 ml/min via a syringe pump (Harvard apparatus 33 DDS) and measure the pressure inside the container with a differential pressure sensor (60 PSI Ashcroft® GV Pressure Transducer). Note that the pressure sensor signal is recorded via a logic analyzer (Saleae Logic pro 8) which is synchronized with the syringe pump.

In addition to the results presented in the main text, we also characterize the effect of both cyclic loading and the loading rate on the pressure-volume characteristics of the metafluid. In order to assess the effect of cyclic loading, we place a capsule with $R_o = 10$ mm and $t = 2$ mm in a container with volume $V_{tot} = 60$ ml and perform 110 loading/unloading cycles. As shown in Fig. S4, we find that pressure volume curves are mostly invariant, except for a small reduction in the critical snapping pressures which decrease by 5 kPa over more than 100 cycles. As such, these results indicate that cyclic loading has a minimal effect on the behavior of metafluids comprising centimeter scale capsules. Nevertheless, it is important to acknowledge that the long-term behavior of the capsules may be influenced by the diffusion of air through their walls, posing a potential source of alteration.
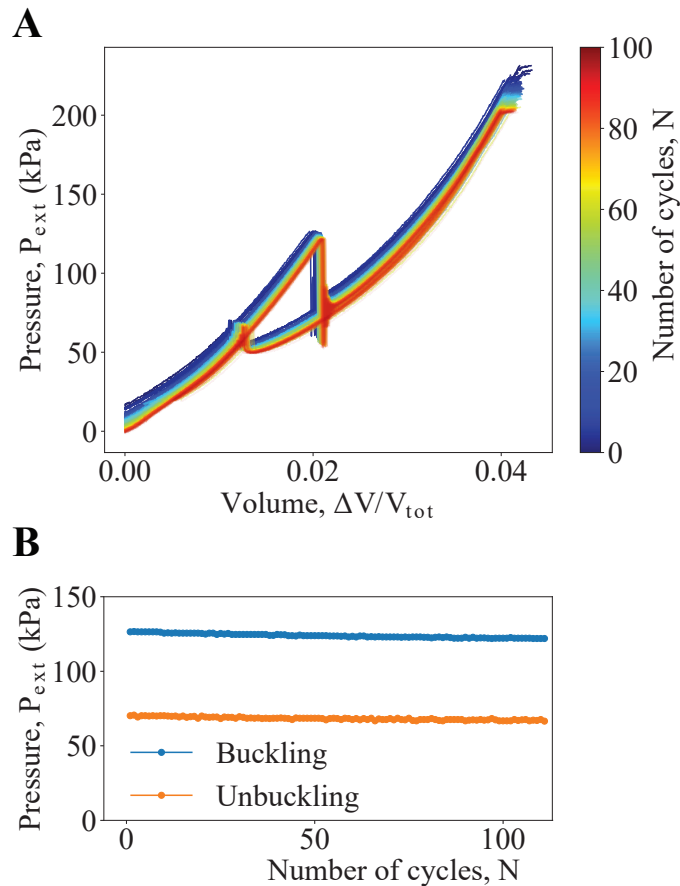

Fig. S4. Cycling loading of a centimeter scale capsule (A) Pressure-volume curve recorded over 100 loading/unloading cycles. (B) Evolution of the critical pressures over the cycles.

To characterize the effect of the loading rate, we place three capsules with $R_o = 10$ mm and $t = 2$ mm in a glass syringe (50 mL Gastight Syringe Model 1050 TLL, PTFE Luer Lock) filled with water. We connect a pressure sensor (60 PSI Ashcroft® GV Pressure Transducer) to the syringe to record the pressure during the experiment and connect the plunger of the syringe to an Instron machine through an acrylic plate. We then use the Instron to push the syringe's plunger and, therefore, pressurize the fluid at displacement rates ranging from 0.01 mm/s to 10mm/s. The results shown in Fig. S6 show that, within the considered range, the effect of the loading rate on the response of the metafluid is negligible.

Note that the testing setup presents a not negligible compliance. To characterize it, we filled the container with $V_{tot} = 250$ mL of pure water (no shells) and measured the pressure while slowly introducing an additional volume of water ΔV. In Fig. S7
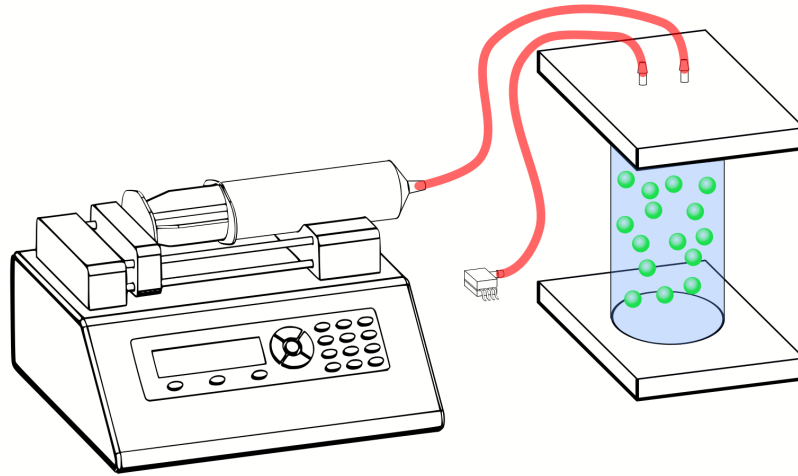
Fig. S5. Pressure-volume curve of the metafluid with centimeter-scale capsules. Schematic of the test setup used to characterize the pressure-volume characteristics of our metafluid with centimeter-scale capsules.
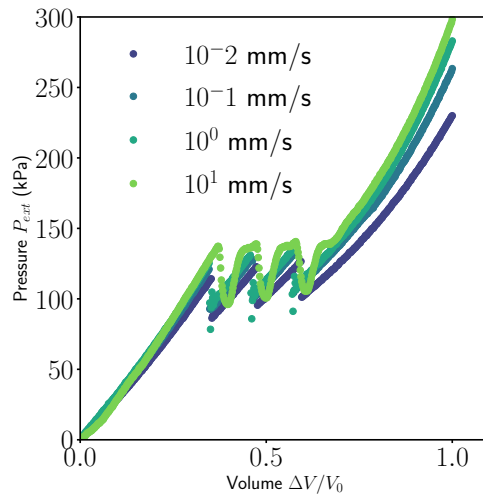
Fig. S6. Effect of loading rate. Pressure-volume curve recorded for different loading rates ranging from 0.01 mm/s to 10mm/s.

we show the pressure-volume curve collected from these test, which we then used in simulations to mimic the experimental conditions (see details in Section S3.1).

Gripper. As shown in Fig. S8A, the gripper used to obtain the results reported in Figure 3A of the main text consists of

- a syringe that contains a volume of fluid ΔV large enough to hold a glass bottle;

- a glass container with $V_{tot} = 100$ mL that we fill with either air, water or the metafluid;

- a syringe connected to the glass container that acts as the moving arm of the gripper;

- a load cell (Futek Miniature S-Beam Jr. Load Cell LSB200.FSH03875) connected to the static jaw that allows us to measure the force experienced by the objects that are grasped. Note that the load cell is connected to an amplifier (Futek Strain Gauge Analog Amplifier with Voltage Output IAA100.FSH03863), whose analog voltage signal is recorded via a logic analyzer (Saleae Logic pro 8).

To demonstrate the concept, we focused on three objects and first measured for each of them the supplied volume required to reach them, ΔV_{reach}, and the pressures needed to hold them, P_{hold}, and crush them, P_{crush} (note that these pressures are obtained by diving the forces measured by the load cell by the cross sectional area of the syringe's plunger). We found that

- for a a glass bottle of 60 mm in diameter and 160 g in weight, $\Delta V_{reach} \approx 1.1$ mL, $P_{hold} \approx 110$ kPa and $P_{crush} \approx 700$ kPa;

- for an an egg of $\approx$25 mm in diameter and $\approx$16 g in weight $\Delta V_{reach} \approx 3.9$ mL, $P_{hold} \approx 12$ kPa and $P_{crush} \approx 105$ kPa;
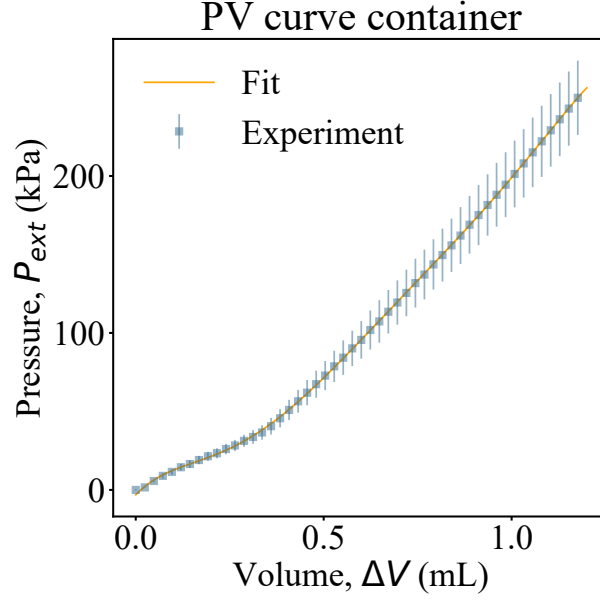
Fig. S7. Compliance of the container. Pressure-volume curve measured when the container is filled with pure water.

- for a blueberry of ≈10 mm in diameter and ≈0.5 g in weight $\Delta V_{reach} \approx 5.1$ mL, $P_{hold} \approx$ and 1 kPa and $P_{crush} \approx 55$ kPa.

Having determined ΔV_{reach}, P_{hold} and P_{crush}, the volume ΔV to be supplied to the system to successfully grasp an object can be easily identified by shifting horizontally by ΔV_{reach} the pressure-volume curve for the considered fluid and then identifying the volumes for which $P_{hold} \leq P_{ext} \leq P_{crush}$ (see Fig. S8B). We find that (*i*) for air 195 mL $\leq \Delta V \leq$ 308 mL, 91 mL $\leq \Delta V \leq$ 190 mL and 68 mL $\leq \Delta V \leq$ 155 mL to successfully grasp the bottle, the egg and the blueberry, respectively; (*ii*) for water 0.5 mL $\leq \Delta V \leq$ 0.99 mL, 3.8 mL $\leq \Delta V \leq$ 4.2 mL and 4.8 mL $\leq \Delta V \leq$ 5.0 mL to successfully grasp the bottle, the egg and the blueberry, respectively; (*iii*) for the metafluid 6.6 mL $\leq \Delta V \leq$ 11.1 mL, 4.7 mL $\leq \Delta V \leq$ 10.7 mL and 5.1 mL $\leq \Delta V \leq$ 8.4 mL to successfully grasp the bottle, the egg and the blueberry, respectively (these regions are highlighted in red, yellow and blue in Fig. S8B). These results clearly show that a different ΔV is required to successfully grasp all three objects when using water and air. Differently, if we use the metafluid and choose 6.6 mL $\leq \Delta V \leq$ 8.4 mL we can successfully grasp all three objects with the same ΔV. As shown in Fig. S8C, when we use air and supply $\Delta V = 218$ mL, we can successfully grasp the bottle, but we crush the egg and the blueberry. Similarly, if we use water and supply $\Delta V = 0.5$ mL, we can successfully grasp the bottle, but we don't reach the egg and the blueberry. Differently, if we use the metafluid and supply $\Delta V = 6.7$ mL, we can successfully grasp all three objects.

Logic gates.   Reconfigurable logic elements can be realized by taking advantage of the sudden change in ΔV triggered at P_{cr}^{up} under pressure controlled conditions. Towards this end, we first exploit the highly nonlinear response of our metafluid to design a tunable flow switch. Such switch is realized by connecting a syringe to a container with $V_{tot} = 100$ ml filled with our metafluid and attaching a blade to its plunger flange (Fig. S9C-(i)). We then connect an elastomeric tube to the syringe's barrel flange and use a pressure controller (Fluigent Flow EZ™ 7bar) to apply P_{in} to the the external side of the syringe's plunger. As P_{in} is increased, the plunger and blade move by ΔX until the blade flattens the soft tube and completely stops the flow through it (for $\Delta X = 28$ mm). It is important to note that the characteristics of this switch are determined by the properties of the metafluid in the container. To demonstrate this point, we consider three metafluids with: ($M1$) $K_0 = 0.9$ MPa and $P_{cr}^{up} = 45$ kPa (realized by filling the with water and 12 shells with $G = 60$ kPa, $t = 2$ mm and $R_o = 10$ mm); ($M2$) $K_0 = 18$ MPa and $P_{cr}^{up} = 120$ kPa (realized by filling the container with water and one shell with $G = 350$ kPa, $t = 2$ mm and $R_o = 10$ mm); and ($M3$) $K_0 = 140$ MPa and $P_{cr}^{up} = 590$ kPa (realized by filling the container with water and one shell with $G = 350$ kPa, $t = 4.5$ mm and $R_o = 10$ mm). As shown in Fig. S9C-(ii), the initial bulk modulus of metafluid $M1$ is low enough to make the switch close before $P_{in} = P_0 = 45$ kPa (pink line), whereas that of metafluid $M3$ is large enough to keep it open both at P_0 and $P_{in} = P_1 = 120$ kPa (blue line). Differently, for metafluid $M2$ the snapping of the capsule triggers a large ΔX that suddenly stops the flow through the soft tube at $P_1 = 120$ kPa (green line). Next, we combine switches based on these three metafluids to design reconfigurable logic gates. In particular, we consider two soft tubes both connected at their end to a balloon (which allows us to read the state of the gate) and to a pressure supply and distribute three switches along them (Figs. S9C-(iii) and S9C-(iv)). Note that two switches are actuated by the same input pressure P_{in}^A and the third one by P_{in}^B. If we define input logical states 0 and 1 as $P_{in} = P_0$ and $P_{in} = P_1$, respectively, we can realize a NOR gate by connecting the two switches arranged in series on one of the soft tubes to metafluid $M2$ and the other one to metafluid $M1$
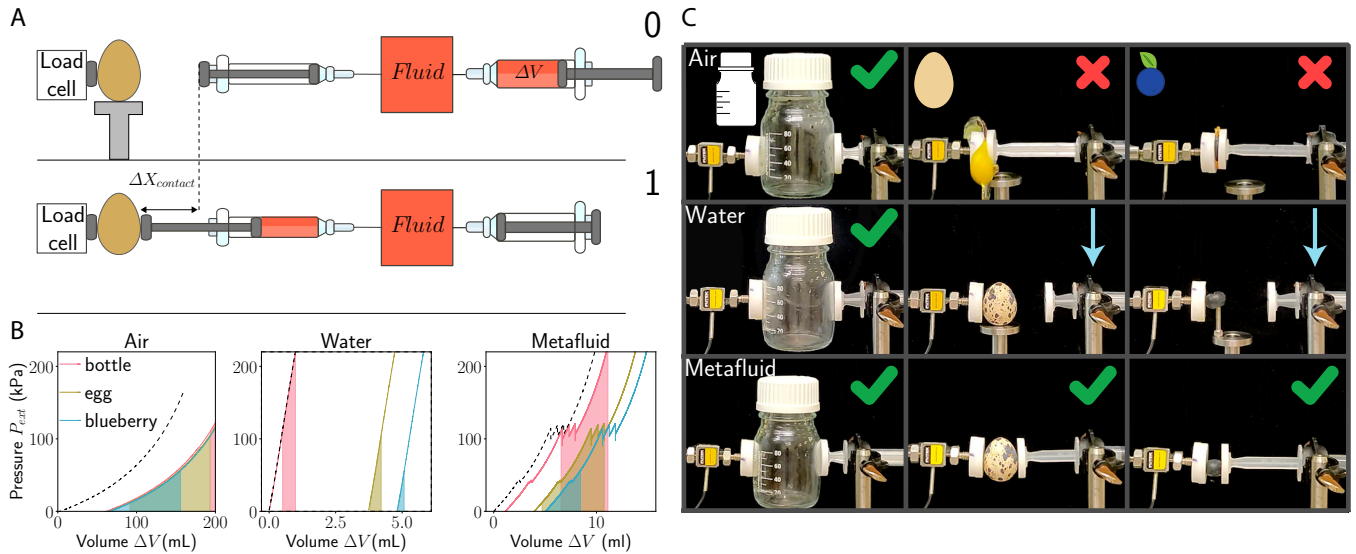
Fig. S8. Gripper (A) Schematics of the experimental setup. (B) To identify the volume ΔV to be supplied to the system to successfully grasp an object, we shift the pressure-Volume curve of the considered fluid (black dashed line) horizontally by ΔV_{reach} for that object. The range of ΔV that enable successful grasping of the bottle, egg and blueberry are highlighted in red, yellow and blue, respectively. (C) Snapshots of the gripper after injection of ΔV = 218, 0.5 and 6.7 mL for air, water and metafluid. The green check mark, the blue down arrow and the red cross indicate successful grasping, dropping and crushing, respectively.

(Fig. S9C-(iii)). Remarkably, the very same system becomes a logical NAND gate when we simply replace $M1$ with $M2$ and $M2$ connected to P_{in}^A with $M3$ (see snapshots in Fig. S9C-(iv)). It should be noted that, since both NAND and NOR gates are functionally complete, they can be combined to construct many other logic circuits whose function can be reprogrammed by simply changing the metafluid connected to the switches. These findings highlight a key benefit of employing metafluids in logic gates: the ease with which the fluid can be replaced, allowing for the reprogramming of circuit functionality.

S2.2. Metafluid with micrometer-scale capsules.

Pressure-volume curve of a single microcapsule.   To measure the pressure-volume curve of a single micrometer-scale capsule (as shown in Figure 1E of the main text), we place the capsule in a micro-liter glass syringe (Hamilton®25 μL Model 802) filled with immersion oil (Cargille immersion oil type A). Note that, to reduce the distortion caused by the glass syringe and obtain a clear image of the capsule with minimal optical errors, we submerge the syringe in a larger transparent container filled with the same immersion oil. In our experiments, the volume inside the syringe is controlled by mechanically connecting the syringe's plunger to a high precision linear stage (PI®PLS-85, controlled via a motion controller - PI®SMC Hydra Motion Controller). The deformation of the capsule is then visualized by using a high speed camera (Phantom/Ametek TMX 5010) connected to a 200 mm focal length tube lens (Thorlabs AC254-200-A-ML - f=200 mm) and a long working distance objective (10X Mitutoyo Plan Apo Infinity Corrected Long WD Objective). To measure the pressure P_{ext}, we inject an air bubble with a diameter of ≈ 370 μm in into the syringe and monitor the evolution of its volume when the syringe's plunger moves. More specifically, we extract the shape of the bubble from the recorded videos and fit it to a sphere. We then calculate the pressure as

$$P_{ext}(t) = \frac{P_0 V_{bubble}(0)}{V_{bubble}(t)},$$

where P_0 is the initial (atmospheric) pressure and $V_{bubble}(t)$ is the volume of the air bubble at time t. Finally, we note that, to correct for the presence of the bubble, we subtract V_{bubble} from the volume change imposed by the syringe's plunger.

Pressure-volume curve of a microsuspension.   The results presented in Figure 1F of the main text are for a micro suspension obtained by mixing microcapsules with external radius $R_o = 250$ μm and thickness $t \approx 65$ μm together with glycerol (99% pure, Sigma Alrich). In our experiment, a 10 mL syringe is filled with a solution with initial capsule volume fraction $\varphi = 0.3$. The syringe's plunger is slowly displaced to reduce the enclosed volume by ΔV, while keeping the tip closed with a 3-way valve (Luer-lok) and monitoring pressure with a pressure sensor (60 PSI Ashcroft® GV Pressure Transducer).

Optical properties of the microsuspension.   Two set of experiments were conducted to investigate the optical properties of the microsuspension: one to characterize its transmittance as function of the applied pressure and the other to qualitatively investigate the light scattering as function of the applied pressure. For both experiments, we used the microcapsules considered in Figure 1F of the main text suspended in a silicone oil (Polydimethylsiloxane, Trimethylsiloxy terminated, CAS No: 9016-00-6/63148-62-9, GELEST Inc.) with $\varphi \approx 0.4$.

   To characterize the transmittance, we loaded 1 mL of the microsuspension in a 3mL plastic syringe (Becton-Dickinson). For the experiments, which were conducted in a dark room, we positioned a fiber-coupled Helium-Neon laser with red light
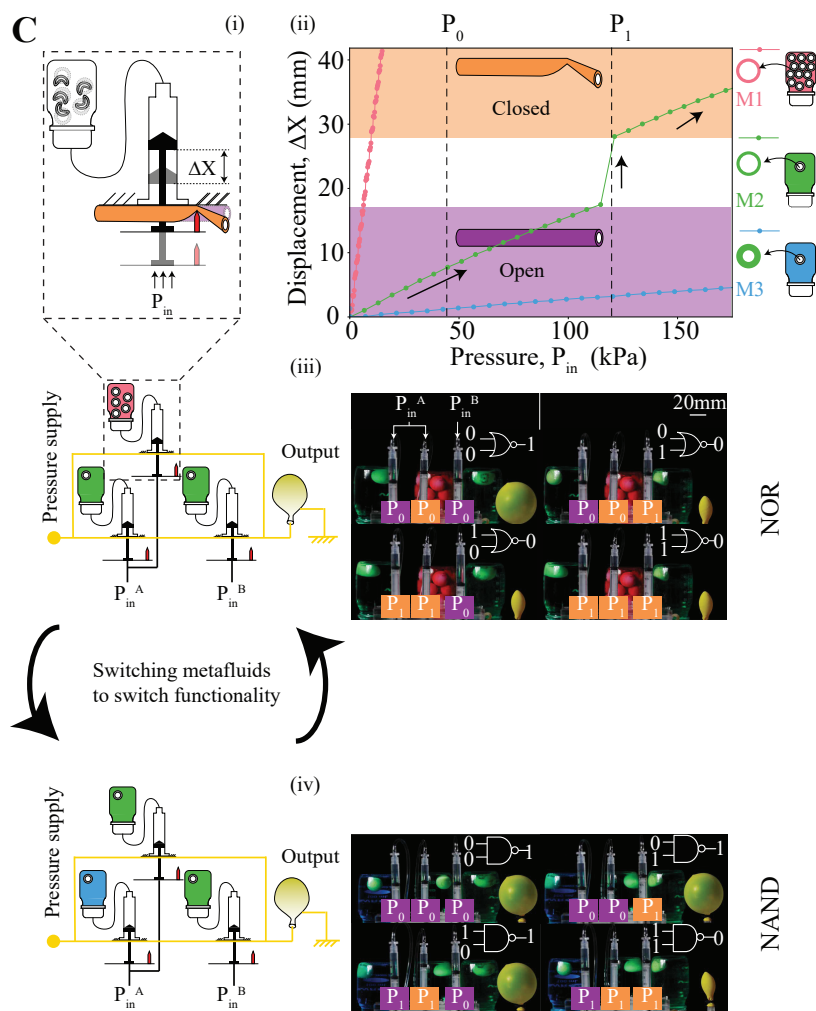
Fig. S9. Reconfigurable logic gates: (i) Schematics of the tunable flow switch. Color indicates state: orange closed, purple open. (ii) Characterization of the switch with different metafluids: $M1$ (pink) with $K_0 = 0.9$ MPa and $P_{cr}^{up} = 45$ kPa; $M2$ (green) with $K_0 = 18$ MPa and $P_{cr}^{up} = 120$ kPa; $M3$ (blue) with $K_0 = 140$ MPa and $P_{cr}^{up} = 590$ kPa. (iii) Schematics of a NOR gate and snapshots. If the balloon is inflated the output of the gate is 1, otherwise it is 0. (iv) Schematics of a NAND gate and snapshots.
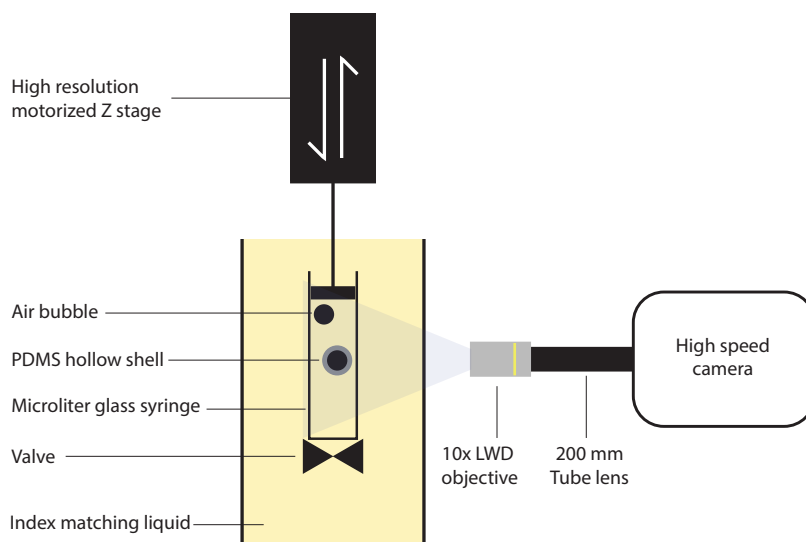
Fig. S10. Testing of a single micrometer-scale capsule. Schematic of the setup used to characterize the pressure-volume characteristics of a single microcapsule.

163 (wavelength 633 nm, Newport N-LHR-121) in front of the syringe and a laser power meter (Thorlabs S170C) on its back (see Fig. S11).
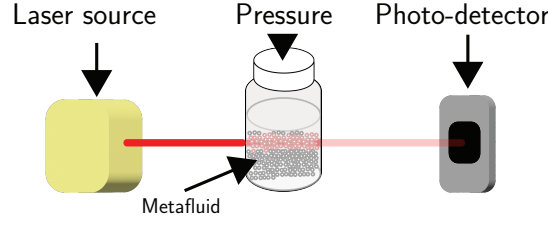
Fig. S11. Optical transmittance of the metafluid. Schematic of the test setup used to characterize the optical properties of metafluid as function of pressure.

164

165 We used a collimator (Thorlabs TC12FC-633) to align the laser and measure the transmittance power with the power meter.
166 Note that we used a pressure pump (Flow EZ^{TM} 7 bar, FLuigent Inc.) to apply a constant pressure to the microsuspension
167 and performed 15 tests at different levels of P_{ext} (we used $P_{ext} = 0, 500, 1000, 1500,..., 7000$ mbar). For each P_{ext}, we recorded
168 ten instantaneous power readings. Further, we also measured the transmitted power when the syringe was filled with pure
169 silicone oil and when the laser was off, both at atmospheric pressure. The transmitted power T of the metafluid relative to that
170 of pure silicone oil was then computed as

$$T(P_{ext}) = \frac{P_{mf}(P_{ext}) - P_{off}}{P_{oil} - P_{off}} \qquad [S1]$$

171

172 where $P_{mf}(P_{ext})$ is the measured power for the microsuspension at P_{ext}, P_{off} is the recorded power with the laser off, and P_{oil}
173 is the transmitted power with pure silicone oil in the syringe. To quantify the uncertainty on the measurements, we calculated
174 the standard deviation of the relative transmittance, σ_T, as

$$\sigma_T^2 = \left(\frac{\partial T}{\partial P}\right)^2 \sigma_{P_{mf}}^2 + \left(\frac{\partial T}{\partial P_{off}}\right)^2 \sigma_{P_{off}}^2 + \left(\frac{\partial T}{\partial P_{oil}}\right)^2 \sigma_{P_{oil}}^2, \qquad [S2]$$

175

where $\sigma_{P_{mf}}$, $\sigma_{P_{off}}$ and $\sigma_{P_{oil}}$ denote the standard deviation of the power measured for the metafluid, when the laser was off and for PDMS oil, respectively. Substitution of Eq. (S1) into Eq. (S2) yields

$$\sigma_T^2 = \left(\frac{1}{P_{oil} - P_{off}}\right)^2 \sigma_{P_{mf}}^2 + \left(\frac{P_{mf} - P_{oil}}{(P_{off} - P_{oil})^2}\right)^2 \sigma_{P_{off}}^2 + \left(\frac{P_{off} - P_{mf}}{(P_{off} - P_{oil})^2}\right)^2 \sigma_{P_{oil}}^2.$$

176 To characterize the scattering, we fabricated a 70×70×26.6 mm transparent pressure cell using a combination of laser
177 cutting and milling. More specifically, we used two 0.5" acrylic plates (in which a groove for a 1.54" ID O-ring was added)
178 separated by 1.2 mm acrylic plate that acts like a spacer and allows for the creation of a chamber. Small holes were made
179 in the upper plate to host two 14 gauge blunt tip needles that were used to introduce the fluid and degas the pressure cell.
180 We assembled the pressure cell with 8 screws and filled it with our microsuspension. We then used a pressure pump (Flow
181 EZ^{TM} 7 bar, FLuigent Inc.) to control the pressure inside the cell and perform a pressure sweep from 0 to 7000 mbar. In our
182 experiment, we placed a Harvard logo under the pressure cell and used a camera (Canon 90D) positioned above it to record to
183 the logo as the pressure in the pressure cell was increased.
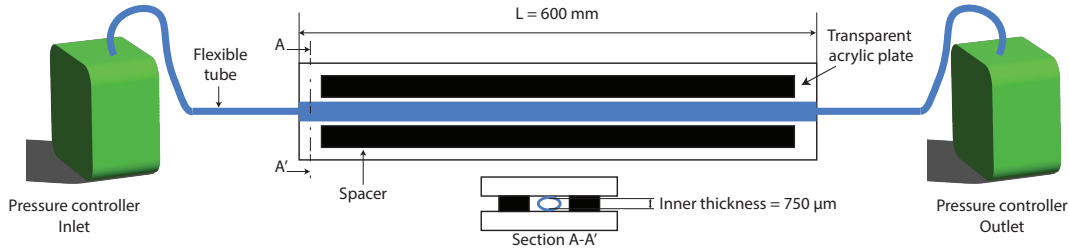
Fig. S12. Flow of the microsuspension. Schematic of the test setup used to characterize the flow of the metafluid.

184 **Flow of the microsuspension.** To characterize the flow of our metafluid, we built an experimental setup that consists of a flexible
185 tube of inner and outer diameter of 3/32" and 5/32" and a length of 1.2 m that is squeezed between two acrylic plates spaced
186 by 1/16". to account for the tube thickness plus 750 μm. This gives the tube an elliptical gross section with major axis $a_{ch} =3$
187 mm and minor axis $b_{ch} =750$ μm. As shown in Fig. S12, the tube is connected on both ends to reservoirs, themselves connected
188 to a pressure controller (Fluigent Flow EZ 7 bar pressure controller). For this set of experiments we used capsules with outer
189 radius $R_0 = 250$ μm and thickness $t = 75$ μm that snap at $P_{cr}^{up} \approx 300 \pm 20$kPa. In particular, we tested two fluidic media:

- a solution of pure silicone oil with a kinematic viscosity $\nu = 100cSt$ (Polydimethylsiloxane, Trimethylsiloxy terminated, CAS No: 9016-00-6/63148-62-9, GELEST Inc.) which is the base solution ($\varphi = 0\%$).

- a suspension obtained by mixing pure silicone with microcapsules with external radius outer radius $R_0 = 250\ \mu m$ and thickness $t = 75\ \mu m$ and buckling pressure $P_{cr}^{up} \approx 300 \pm 20$kPa. Note that we considered two values of capsule volume fraction: $\varphi = 0.1$ and 0.3.

In our experiments, we fixed the difference of pressure between the inlet and outlet to be $\Delta P = P_{in} - P_{out} = 50$ kPa and considered $P_{in} \in [50, 450]$ kPa. We monitored the flow front using a camera (Phantom TMX 5010 high speed camera) and then calculated its average velocity once the flow was fully developed, $\overline{v}_{front}$. In Fig. S13, we show the extracted average velocity front (normalized by the average velocity front at $P_{in} = 50$ kPa) as a function of P_{in} for metafluids with $\varphi = 0$ (pure fluid), 0.1 and 0.3. Note that the shear rate experienced by the metafluid in all these tests can be estimated as

$$\dot{\gamma} \approx \frac{\overline{v}_{front}}{0.5D_h} \tag{S3}$$

where $\overline{v}_{front}$ is the measured front speed reported in Fig. S13. Further, D_h denotes the hydraulic diameter, which is given by

$$D_h = \frac{4A}{\Pi}, \tag{S4}$$

where $A = \pi a_{ch} b_{ch} = 1.77$ mm^2 is the cross sectional area of the channel and Π is its perimeter, which for an ellipse can be approximated as

$$\Pi \approx \pi \left[3(a_{ch} + b_{ch}) - \sqrt{(3a_{ch} + b_{ch})(a_{ch} + 3b_{ch})} \right] = 6.43\,mm \tag{S5}$$

By using $\overline{v}_{front}^{spherical} = 1.65$ mm/s and $\overline{v}_{front}^{collapsed} = 1.05$ mm/s, we obtain $\dot{\gamma} \approx 1.5$ s^{-1}. and $\dot{\gamma} \approx 0.95$ s^{-1} for the metafluid with spherical and collapsed capsules, respectively.

To record the microscopic images reported in Fig. 4 of the main text, we relied on the same optical system presented in Fig. S10.
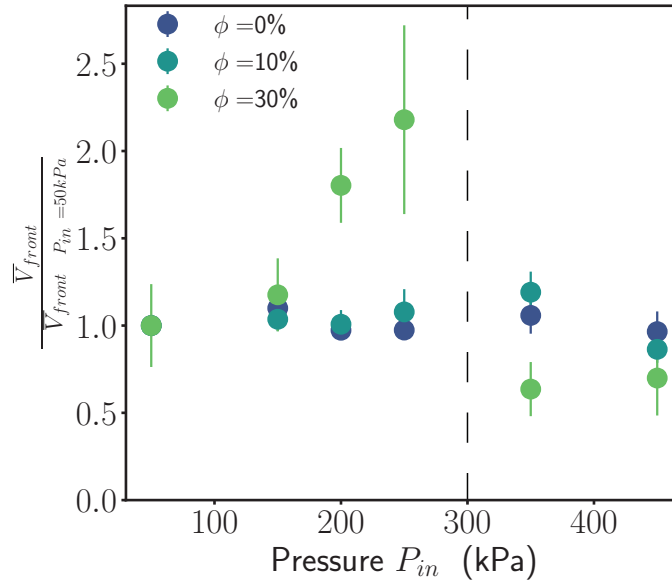
Fig. S13. Measurements for pressure driven flow at constant $\triangle P = 50$ **kPa** Average velocity front (normalized by the average velocity front at $P_{in} = 50$ kPa) as a function of P_{in} for metafluids with $\varphi = 0$ (pure fluid), 0.1 and 0.3.

Rheology of the microsuspension. To better understand the impact of capsule shape on the flow of metafluid, we characterize its rheology using a parallel plate rheometer (TA instruments Discovery HR 30) with two disks of 50 mm diameter separated by a gap of 500 μm. In all our tests, at room temperature (20 °°C) we applied a ramp of increasing shear rate $\dot{\gamma}$ and swept it logarithmically from $1\,\text{s}^{-1}$ to $100\,\text{s}^{-1}$ with five points per decade and an averaging time of 30 s. We first performed the test with increasing shear rate and then repeated it in decreasing order to check the reproducibility of the measurements. Note that the reported results are the average of the two tests, the variability measured is typically of the order of 3 % of the average value at a given shear rate. Since using this setup we were unable to control external pressure applied to the metafluid, we prepared two suspensions:

- (i) a suspension with 30% volume fraction of spherical microcapsules (with $R_o = 40\ \mu m$ and $t = 8\mu m$) in silicone oil. Note that the miscrocapsules are fabricated following all steps shown in Fig. S3;

- (*ii*) a suspension with collapsed particles in silicone oil. To obtain the collapsed particles, we prepared the same volume of spherical capsules (with $R_o = 40 \ \mu m$ and $t = 8 \mu m$) as in (i) but this time we followed the process described in Fig. S3 up to Step 3. After that, we dried the inner core by evaporation (instead of sublimation), causing them to collapse permanently. The collapsed shells where then re-suspended in silicone oil to match the volume fraction of the first solution after collapse (upon pressurization).

In addition to these two suspensions, we also tested pure silicone oil (the solvent used for the two tested suspensions). The results are shown in Fig. S14A and indicate that the silicone oil behaves as a Newtonian fluid with viscosity $\eta_0 \approx 0.1$ Pa.s.

Finally, we performed oscillation sweeps with frequency $\omega \in [0.1, 10]$ Hz at low strain amplitudes (3% to remain in the linear-viscoelastic region) to probe the viscoelastic behavior of the metafluid with spherical and collapsed particles. As shown in Fig. S14B, we find that the suspension with spherical microcapsules is dominated by viscous effects which are linear with ω. Differently, the suspension with collapsed microcapsules behaves like a viscoelastic solid at low frequencies ($\omega < 1Hz$) where G' dominates. For $\omega > 1Hz$, the dominance of G'' indicates that viscous effects prevail in the metafluid.
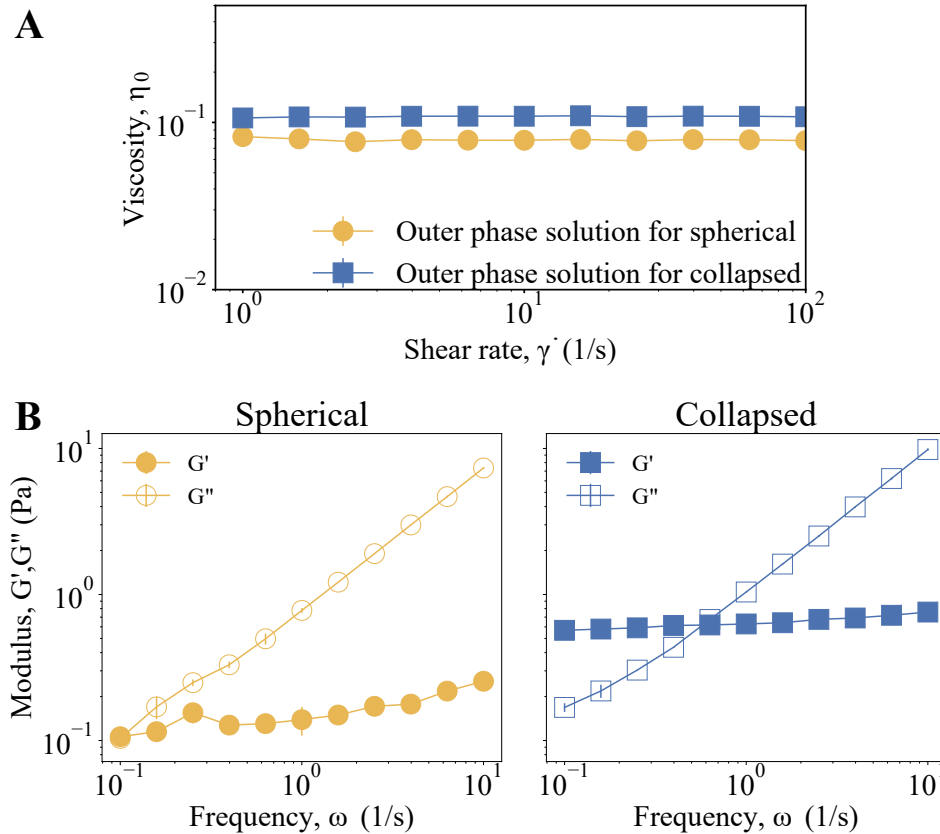
Fig. S14. Rheological measurements of the micro-suspensions. **(A)** Shear rate measurement of the outer phases used for the solutions comprising spherical and collapsed micro-capsules. **(B)** Oscillation sweep in frequency for micro-suspensions comprising spherical and collapsed micro-capsules.

S3. Modeling

In this Section, we first describe the simulations conducted to characterize the response of individual capsules and then explain how we model the interactions between them.

S3.1. FE simulations of individual capsules. To model the behavior of single capsules under hydrostatic pressure loading, we first conduct a finite element (FE) simulation in Abaqus (Abaqus/CAE 2020, Dassault Systèmes) and then account for the contribution of the compressible gas inside the capsule.

Geometric model. The geometry of our spherical capsules is fully defined by two parameters: the outer radius R_o and the thickness t. Following the framework of thin shell theory, we can then express these in terms of the midline radius R and the dimensionless thickness η (Fig. S15A) as

$$R_o = R \left(1 + \frac{\eta}{2}\right), \quad t = \eta R. \qquad [\text{S6}]$$

Note that η is the ratio between the thickness of the shell and R and always lies in the interval $]0, 2[$, since for $\eta = 0$ the shell has no thickness and for $\eta \geq 2$ the shell has no inner surface.

For the capsules analyzed in this study, R ranges from 10^{-2} m for the centimeter scale capsules to 10^{-5} m for the micrometer scale capsules in which the smallest feature size is below 10^{-6} m. Since in Abaqus the smallest length scale supported by the geometry engine is 10^{-6} (2), the dimensions of the capsule can not be expressed in SI units in the software. Therefore, we scale the simulation geometry uniformly to $R = 1$ and represent all other geometric parameters as dimensionless fractions of R. The dimensionless simulation results are then transformed back to SI units in a post-processing step.
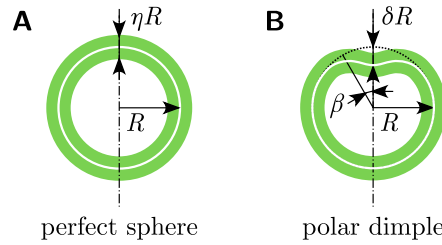

Fig. S15. Shell simulation geometry. Cross-sections of a spherical capsule before (A) and after (B) applying a polar dimple imperfections.

When using a perfect sphere, the FE simulations can only produce spherically symmetric deformations. In physical spherical capsules, however, the deformation in response to a uniform pressure loading is only spherically symmetric up to the critical pressure. At that pressure small imperfections in the geometry destabilize the uniform deformation and a dimple forms that breaks the spherical symmetry. To reproduce this behavior reliably in our simulations, the stress-free base geometry is perturbed by a small dimple, as shown in Fig. S15B. More specifically, this dimple is generated by radially displacing every point throughout the shell with the field (3)

$$\frac{\vec{\delta}_{dimple}}{R} = -\delta e^{-(\phi/\beta)^2} \vec{r}, \qquad [\text{S7}]$$

where the dimensionless numbers δ and β describe the dimple depth and width, respectively, $\vec{r}$ is the vector pointing from the center of the sphere to the point on the shell and ϕ is the angle between r and an axis going through the center of the shell. This localizes the formation of a dimple at $\phi = 0$. The point at this angle that lies on the outer surface of the shell is called the pole, while the point on the outer surface at $\phi = \pi$ is called the antipole. Note that for all numerical results presented in the main text we use $\beta = 30°$ and $\delta = 0.005\eta$. When running the same simulations with a larger imperfection of $\delta = 0.02\eta$, the critical pressure P_{cr}^{up} decreases by at most 10% for all shells with $\eta < 1$. As such, we can conclude that $\delta = 0.005\eta$ is large enough to prevent numerical artefacts due to the perfect spherical symmetry but small enough to minimize the distortion of the pressure-volume characteristic.

In our simulations we assume the deformation to be axisymmetric and discretize the models using using four-node bilinear axisymmetric solid elements (element type CAX4H in Abaqus) for shells with $\eta \geq 0.05$ and two-node axisymmetric shell elements (element type SAX1 in Abaqus) for shells with $\eta < 0.05$. The axisymmetric simplification is consistent with the observed deformation of the manufactured capsules in this study. However, it is important to point out that it is only valid for shells that are sufficiently thick. For thin shells, the instability on loading that leads to the formation of a circular dimple at the pole can be followed by a secondary instability in which the edge of the dimple becomes polygonal. This symmetry-breaking secondary instability occurs at a critical volume of approximately (4)

$$\frac{\Delta V_{cr,2}^{up}}{V_0} = 3706 \frac{\eta^2}{12(1 - \nu^2)}, \qquad [\text{S8}]$$

where $V_0 = (4\pi R^3)/3$. Since silicone rubbers can be considered as incompressible, $\nu \approx 0.5$, if follows that $\Delta V_{cr,2}^{up}/V_0 > 1$ for $\eta > 0.05$. This means that for all shells that are of practical relevance in this research the secondary buckling transition does not occur before the shell is fully compressed so that the volume of the internal cavity vanishes (i.e. $\Delta V = V_0$). Therefore, the

assumption of axisymmetric deformation does not introduce an additional modelling error. This is confirmed by the results reported in Fig. S16A, where we compare the pressure-volume response from an axisymmetric and a fully three dimensional simulation for a shell with $\eta = 0.22$. We find that the two responses are indistinguishable for $\Delta V/V_0 < 0.8$. Discrepancies occur if the shell is compressed further and the inner surface makes self-contact (cross-section in the inset of Fig. S16A), but for most practical applications this level of compression is not reached, so axisymmetric simulations are sufficiently accurate and used for this study.

We note that the the computational time could be reduced by using shell elements also for models with $\eta > 0.05$. As shown in Fig. S16B, simulations with shell and solid elements yield identical results for thin shells with $\eta < 0.3$. However, for shells with $\eta \geq 0.3$ the results obtained using shells elements diverge from those obtained using solid elements in the collapsed regime. One reason for this divergence is that the model for the SAX1 elements assumes that the strain in the thickness direction varies weakly over the surface of the shell (5) - an assumption that is violated for thick shells. For example, for the deformation of the shell with $\eta = 0.3$ depicted in the inset in Fig. S16B, the large localized curvature at the inner surface results in thickness variations in the range of 20 % over the entire shell. Moreover, shell elements do not accurately model the spherical regime for $\eta > 0.5$ since the SAX1 shell element formulation also assumes that the strain in the thickness direction is uniform throughout the thickness of the shell (5) - an assumption that is again violated for thick shells. All these results motivasted our decision to use four-node bilinear axisymmetric solid elements (element type CAX4H in Abaqus) for shells with $\eta \geq 0.05$ and two-node axisymmetric shell elements (element type SAX1 in Abaqus) for shells with $\eta < 0.05$.

As for the size of the mesh, we conduct the following mesh size studies to determine the number of elements along the radial direction of the shell, N_r, and the number of elements along the tangential direction, N_t:

Solid elements: We consider a shell with $\eta = 0.22$ and investigate the effect of N_r on its pressure-volume response. Note that we mesh the model with square elements, so that $N_t = R\pi/(R\eta/N_r) = N_r\pi/\eta$. As shown in Fig. S17A, we find that the critical pressure is captured accurately for $N_r = 5$, as the critical pressure changes by only 1.5×10^{-4} % when N_r is further increased. Further, we investigate the effect of changing N_t independently from N_r over a large range. This is only possible for a mesh of shell elements, so the second study concerns a spherical shell with $\eta = 0.22$ meshed with N_t SAX1 shell elements (Fig. S17B). We find that the critical pressure varies by less than 0.1 % for $N_t > 40$. Since the largest curvature occurs at the inner surface of the shell with radius $R_i = (1 - \eta/2)R$, in all simulations with solid elements the mesh size is at most $\pi R(1 - \eta/2)/40$, unless the requirement on N_r that limits the maximum element size to $\eta R/5$ is more strict.

Shell elements: We consider a spherical shell with $\eta = 0.016$ meshed with SAX1 shell elements and systematically vary N_t (Fig. S17C). We find that for small values of N_t the collapsed branch of the pressure-volume characteristic develops ripples with amplitude that decreases with N_t and frequency directly proportional to N_t. These ripples are caused by the high curvature of the rim. As the dimple expands, elements traverse this region of high curvature and the angle between these elements and neighboring elements changes. If N_t is too small, this change in angle is drastic so the total bending energy increases whenever an element traverses the rim. Therefore, the equilibrium pressure increases significantly with a frequency proportional to N_t. As N_t increases beyond $N_t = 50$, the relative amplitude of the ripples decreases below 0.6 % and a more physically accurate characteristic is obtained. Therefore, in all simulations carried out with shell elements, the element size is set to at least $\pi R(1 - \eta/2)/100$.
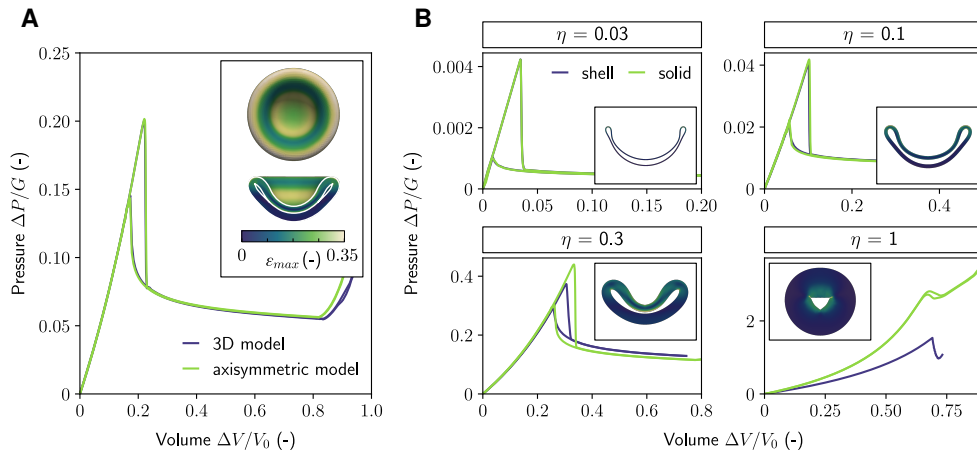
Fig. S16. Shell simulation order reduction. A, Pressure-volume characteristics of a spherical shell with $\eta = 0.22$ modeled using full three-dimensional and axisymmetric continuum elements. The inset shows the top view and the cross-sectional side view of the shell in the fully collapsed state with the color indicating the maximum principal strain. **B**, Pressure-volume characteristics for spherical shells with varying thickness η simulated with axisymmetric solid and shell elements. For the shell with $\eta = 1$, the simulation failed to converge past the critical volume. The insets show the cross-sectional side view of the shell in the fully collapsed state with the color indicating the maximum principal strain.

Material model. To determine hyperelastic material models capable of adequately capturing the response of the silicone rubber used to make the capsules, we perform uniaxial tensile tests on dogbone samples made out of PVS (Green silicone rubber)
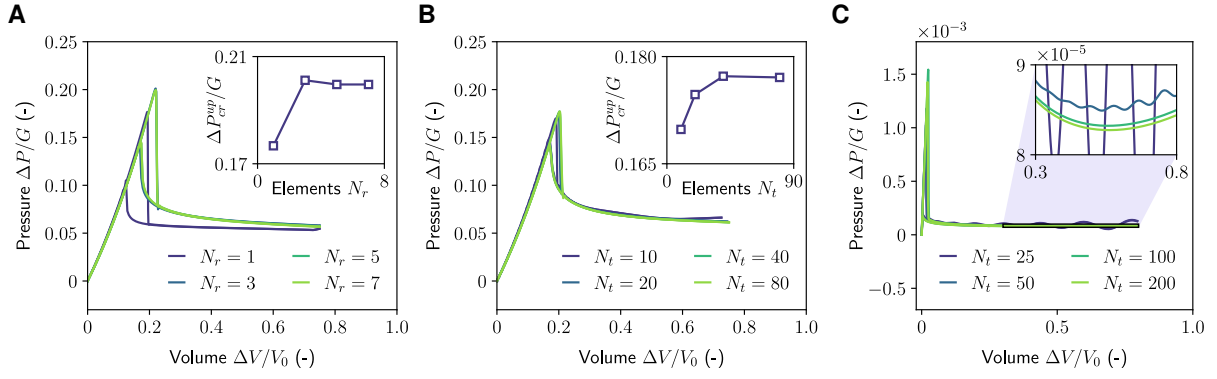
Fig. S17. Mesh size study. A-B, Simulated pressure-volume characteristics for a shell with $\eta = 0.22$ with varying mesh sizes where N_r is the number of solid elements in the radial direction and N_t is the number of shell elements in the tangential direction. The insets show the dependence of the simulated critical pressure ΔP_{cr}^{up} on the number of elements in either direction. **C**, Simulated pressure-volume characteristics for a shell with $\eta = 0.016$ meshed with N_t shell elements. The inset shows the region of the pressure-volume characteristics on loading indicated by the rectangle, zooming in along the pressure axis.

and PDMS. The dobgone samples are fabricated following the ASTM D638 standard tensile testing approach and are loaded by an Instron 5696 at a strain rate of $0.2\,\mathrm{mm/s}$. For the PVS material we find an almost linear relation between true stress and true strain which is accurately captured by fitting a Neo-Hookean model to the data (Fig. S18A). Differently, for PDMS the Neo-Hookean model fails to capture its stress-strain response, but models with two parameters such as the first order Mooney-Rivlin and Ogden models closely follow the data (Fig. S18B). The coefficients that produce the optimal fits for these models are shown in table S1, where $\lambda = 1 + \epsilon$ represents the stretch. Note that all models assume that the material is incompressible. Even though for PDMS the different models produce different estimates for the initial shear modulus of the material G, the pressure-volume characteristics of a PDMS capsule align well when the pressure is normalized by the shear modulus (Fig. S18C). The reason is that for small strains each of the stress-strain relations in table S1 reduces to the linear form $\sigma = 3G\epsilon$ and that the deformed shape of a shell is independent of $\Delta P/G$ (6). This result is consistent with the fact that analytical calculations using different material model formulations yield similar values for the critical buckling pressure of spherical shells (7). Since the assumption that pressure scales with the initial shear modulus suffices for practical purposes, we use a Neo-Hookean model with $G = 1$ in all simulations and report all pressures as the dimensionless group $\Delta P/G$.

Material	Model	Stress-strain relation	Parameters	Shear modulus
PVS	Neo-Hookean	$\sigma = 2C_{10}\left(\lambda^2 - \frac{1}{\lambda}\right)$	$C_{10} = 215\,\mathrm{kPa}$	$G = 430\,\mathrm{kPa}$
PDMS	Neo-Hookean	$\sigma = 2C_{10}\left(\lambda^2 - \frac{1}{\lambda}\right)$	$C_{10} = 306\,\mathrm{kPa}$	$G = 612\,\mathrm{kPa}$
PDMS	Mooney-Rivlin	$\sigma = 2\left(C_{10} + \frac{C_{01}}{\lambda}\right)\left(\lambda^2 - \frac{1}{\lambda}\right)$	$C_{10} = 685\,\mathrm{kPa}, C_{01} = -499\,\mathrm{kPa}$	$G = 371\,\mathrm{kPa}$
PDMS	Ogden	$\sigma = \frac{2\mu}{\alpha}\left(\lambda^\alpha - \frac{1}{\lambda^{\alpha/2}}\right)$	$\mu = 453\,\mathrm{kPa}, \alpha = 4.55$	$G = 453\,\mathrm{kPa}$

**Table S1. Material parameters for both PVS (green rubber) and PDMS.**
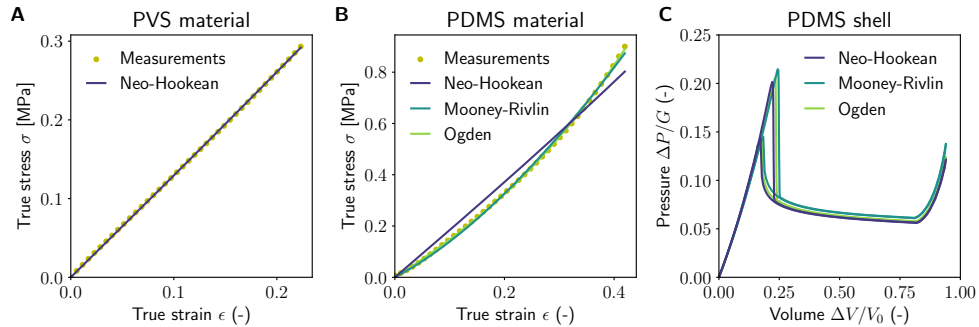
Fig. S18. Material model. (A)-(B) Experimentally measured (markers) and numerically predicted (solid lines) true stress-strain curve for a dogbone sample of (A) PVS and (B) PDMS under uniaxial tension. (C) Simulated pressure-volume characteristics for a shell with $\eta = 0.22$ with the fitted material models for PDMS.

Since the goal of the simulations is to quantify the quasi-static rather than the dynamic behavior of the shells, material properties related to damping and inertia are not based on physical measurements but only serve to stabilize the simulation. Therefore, damping is modeled with the Rayleigh coefficients $\alpha = 0.002\,\mathrm{s}^{-1}$ and $\beta = 0.002\,\mathrm{s}$. These values are sufficient to stabilize the snapping transitions in the simulations and small enough not to distort the quasi-static characteristic. The inertia

of the material is determined by its density ρ which is in the range of $1000\,\mathrm{kg\,m^{-3}}$ for silicone rubber. To preserve the relative contributions of stiffness and inertia to the shell deformation in the simulations with $R = 1$ and $G = 1$, this density needs to be scaled with R^2/G. With a reference value of $R = 10\,\mathrm{mm}$ and $G = 500\,\mathrm{kPa}$, this leads to a dimensionless density of 2×10^{-7}. Because the reference case is a shell on the centimeter scale, this overestimates the contribution of inertia in the micrometer scale shells. However, for a simulation of a shell with $\eta = 0.22$, $R = 1$ and $G = 1$, the peak in kinetic energy during buckling is $17 \times 10^{-6}\,\mathrm{J}$ which is negligible compared to the peak in energy dissipation through the Rayleigh damping of $0.42\,\mathrm{J}$, so inertia has a negligible influence.

Boundary conditions. In all our simulations we fix the vertical coordinate of the bottom node on the axis of revolution and the horizontal displacement and all rotations of the nodes located on the axis of revolution. Further, we include a self-contact interaction to prevent the inner surface of the shell to self-intersect after buckling. This constraint becomes relevant when $\Delta V/V_0$ approaches zero because at that point both poles touch (see inset in Fig. S16). The normal contact behavior is captured by an exponential closure model. In this model, the contact pressure is zero until the gap between two surface elements decreases below 1% of the thickness. For smaller gaps, the contact pressure increases exponentially until it reaches $2G$ when the gap becomes zero. For a sphere with $\eta = 0.22$, this model is sufficient to prevent self-intersection and produces a minimal gap of 0.75% relative to the shell thickness. The tangential contact behavior is modeled as static friction with a coefficient of 1.15 This coefficient is an estimation but it already limits the tangential slip to 0.01% of the shell radius so we conclude that the precise value for the friction coefficient does not have a significant influence on the quasi-static pressure-volume curve.

Loading. To simulate the pressurization and depressurization of the shells, we use implicit dynamic analysis with two steps - one for the loading and one for the unloading. In the simulations we control the volume rather by defining a fluid cavity interaction on the inner surface and applying a load of the type `fluid flux` on this interaction.
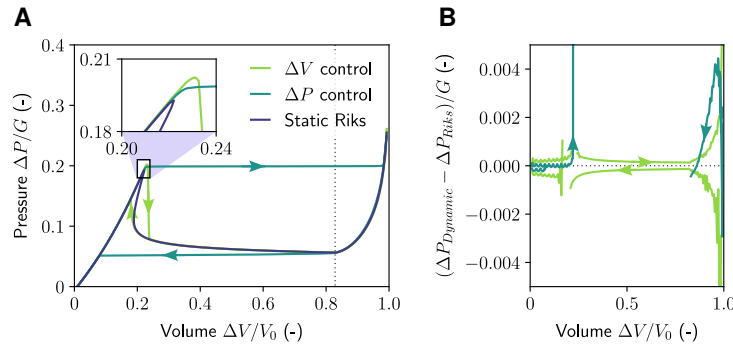
Fig. S19. Finite element model loading. A, Simulated pressure-volume characteristics for a spherical shell with $\eta = 0.22$ for dynamic volume-controlled loading, dynamic pressure-controlled loading and static loading using the Riks method for arc length continuation. The dotted vertical line indicates the change in volume above which the inner surface of the shell makes self contact. The inset shows an enlarged section of the characteristics around the critical point on loading. **B**, Difference in pressure between the dynamic and the static simulation on loading (right pointing arrowhead) and unloading (left pointing arrowhead). This difference is only plotted for the quasi-static segments of the simulation in which the normalized pole velocity $1/R \cdot dy/dt < 1\,\mathrm{s^{-1}}$.

In the loading step the cavity is deflated until less than 5% of the original volume remains and in the unloading step the direction of the flux is inverted until the initial volume of the cavity is restored. The flux magnitude is constant throughout each step, except for the first and last $0.01\,\mathrm{s}$ when it changes linearly from or to zero to avoid excessive accelerations. The dynamic snapping transitions are stabilized numerically by applying Rayleigh damping (as described in section "Material model") and setting the type of the step to moderate dissipation. With a step time of $5\,\mathrm{s}$ for both steps, these measures suffice to ensure convergence. As a final measure to facilitate convergence, a variable time stepping scheme is used. To ensure that the onset of buckling is captured with sufficient resolution in time, the maximum time increment size is limited to $0.03\,\mathrm{s}$.

Note that the highly nonlinear response of the shells could be also captured using arc length continuation in a static simulation step (8) (Fig. S19A). However, simulations using this methods do not converge reliably for thicker shells. Remarkably, when comparing the results of static and dynamic simulations, we find an error for the critical pressure that is less than 1% (Fig. S19), which confirms that the simulation approximates quasi-static loading conditions well. The only exception to this is the region around the critical point on loading, where the dynamic simulation overestimates both the pressure and the volume by approximately 5%. However, since in practical loading scenarios dynamic effects are also present, the results for the dynamic simulation are more accurate than for the static simulation, which is confirmed by the good match between experiments and the numerical model.

Effect of the internal gas. The contribution of the internal pressure caused by the compression of the gas inside the capsule $P_{int}(\Delta V)$ is calculated by a post-processing algorithm operating on the simulation results as

$$P_{int}(\Delta V) = P_0 \left(\frac{1}{1 - \frac{\Delta V}{V_0}} - 1 \right) \qquad [S9]$$

with P_0 atmospheric pressure (101.325 kPa) and V_0 the internal volume of the capsule when it is exposed to atmospheric pressure at the outside. Both contributions are then added to obtain the relation between the external pressure on the capsule and the change in volume as

$$P_{ext}(\Delta V) = \Delta P_{shell}(\Delta V) + P_{int}(\Delta V) \qquad \text{[S10]}$$

This approach allows to examine the influence of a large number of parameters on the deformation of spherical capsules with a minimal number of simulations. It also shows that, in contrast to structures that are inflated from the inside and of which the outside is exposed to atmosphere, the effective pressure P_{ext} to obtain a certain deformation does not scale linearly with the shear modulus of the capsule wall G (Fig. S20). The reason is that even though $\Delta P_{shell}(\Delta V)$ scales linearly with G as demonstrated in the previous paragraph on the material model, P_{int} only depends on the properties of the gas inside the capsule which are independent of G. Therefore, we do not normalize the pressure axis when reporting P_{ext}. Instead, it is possible to convert the pressure P_{ext} for a capsule with a given shear modulus G and a given change in volume ΔV to the pressure P_{ext}^* of a capsule with the same geometry and ΔV but a different shear modulus G^* using the equation

$$P_{ext}^*(\Delta V) = \frac{G^*}{G} P_{ext}(\Delta V) - \left(1 - \frac{G^*}{G}\right) P_{int}(\Delta V) \qquad \text{[S11]}$$

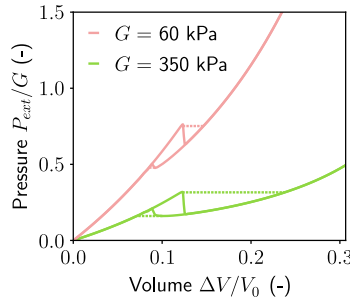where $P_{int}(\Delta V)$ can be obtained from Eq. (S9).

Fig. S20. Dependency of the total pressure on the shear modulus. Pressure-volume curves for capsules with $t/R = 0.22$ and $G = 60$ and 350 kPa where the pressure-axis is normalized by G and the volume axis by the initial external volume of the capsule $V_0 = 4\pi R^3/3$.

Data processing. After calculating the total external pressure due to the shell stiffness and the internal gas pressure, we extract the portions of the pressure-volume characteristic of the capsules that are statically stable in the spherical and collapsed configuration. Since the spherical branch becomes unstable due to a bifurcation in the energy landscape at $(\Delta V_{cr}^{up}, P_{cr}^{up})$, this point appears as a local maximum in pressure in the dynamic volume-controlled simulation. Therefore, the first branch contains the data from all time increments in the loading step of the simulation up to the point where P_{ext} starts decreasing. The collapsed branch, on the contrary, loses stability because of a limit point in volume at ΔV_{cr}^{down}, as shown on the pressure-volume characteristic obtained from the static Riks simulation in Fig. S19A. Since this point does not coincide with a local extremum in pressure, we identify it based on the velocity of the pole in the axial direction $d\Delta y/dt$. This velocity increases significantly at the unstability because elastic energy is released and converted into kinetic energy. Therefore, the end of the collapsed branch is as the increment at which $d\Delta y/dt$ becomes larger than ten times the typical velocity in the quasi-static region of the simulation. This typical velocity is calculated as the average of $d\Delta y/dt$ over the time interval starting at the increment where the two poles break contact and ending at the increment where the cavity volume exceeds ΔV_{cr}^{up} because in this region the pole is always in motion and the simulation is always stable.

After this procedure, the pressure and volume of the critical points on loading and unloading under volume control and loading under pressure control are known. Next, the critical point on unloading under pressure control is found as the local minimum P_{cr}^{down} on the collapsed branch. Due to numerical artefacts caused by the self-contact interaction, multiple local minima in pressure exist that do not correspond with a physical instability threshold. This numerical noise has a high frequency and mostly occur when the shell is nearly in the fully collapsed state. Therefore, we identify P_{cr}^{down} as the point on the quasi-static collapsed branch with the lowest ΔV that has the lowest pressure of the eight points on the branch that lie closest to it in volume and that has a lower pressure than at least half of the data points on the collapsed branch. This algorithm also finds P_{cr}^{down} in case it occurs at the same time increment as ΔV_{cr}^{down}, which is the case when the shear modulus G is low compared to the initial gas pressure $P_{int,0}$.

Model validation. To validate the results of the FE simulations, in Fig. 1B of the main text we compare the numerically predicted and experimentally measured pressure-volume curve of an individual capsule. As described in Section S2.1, in our experiment a capsule is inserted into a container containing a fluid and then a known volume of fluid ΔV is injected into the container while the pressure P_{ext} is monitored. Since our testing setup presents a not negligible compliance

$$\Delta V(P_{ext}) = \Delta V_{cap}(P_{ext}) + \Delta V_{corr}(P_{ext}) \qquad \text{[S12]}$$

where ΔV_{cap} is the change in external volume of the capsule and ΔV_{corr} is the change in volume of all other parts of the system at P_{ext}, assuming that the pressure is uniform. ΔV_{corr} is experimentally characterized (see Fig. S7), whereas our FE simulations provide $\Delta V_{cap}(P_{ext})$. We then use Eq. (S12) to obtain the numerically predicted pressure-volume curve to compare to experiments. As shown by Fig. 1B, after this correction the numerical results align closely with the measurements.

As an additional validation of the numerical model, we compare the results of the numerical model to numerically measured values for P_{cr}^{up} and P_{cr}^{down}. To this end, we manufacture centimeter-scale capsules following the procedure of section S1.1 with $R_o = 10$ mm and with different values for their thickness t following the values of table S2. For each value of t, we manufacture N capsules from the same material. We then measure the critical pressures P_{cr}^{up} and P_{cr}^{down} for all N shells with the same geometry and take their average to produce the values in table S2 and Fig. 2B featured in the main text. Next, we use our model to estimate the values for P_{cr}^{up} and P_{cr}^{down} numerically for the same values of t and R_o. In all these simulations, we keep the material shear modulus $G = 350$ kPa and the imperfection magnitude $\delta = 0.025$ constant to avoid overfitting the simulation data to the experimental results. Therefore, the good match between the numerical and experimental data for P_{cr}^{up} and P_{cr}^{down} reported in table S2 and Fig. 2B demonstrates the predictive power of our numerical model.

Parameters			Average experimental results		Numerical results	
R_o (mm)	t (mm)	N	P_{cr}^{up} (kPa)	P_{cr}^{down} (kPa)	P_{cr}^{up} (kPa)	P_{cr}^{down} (kPa)
10	1.0	4	28.1	15.7	21.8	12.4
10	2.0	4	123.0	57.6	97.5	56.7
10	2.3	8	159.9	76.9	137.1	78.4
10	2.5	8	174.8	83.2	166.8	96.4
10	3.0	8	289.9	150.5	260.1	152.5
10	4.0	6	524.8	343.2	498.9	336.7
10	4.5	4	598.0	473.2	649.1	474.1
10	5.0	6	800.9	632.1	796.8	615.7

Table S2. Comparison between numerical and experimental values for the critical pressures

Effect of bulk modulus. It is well known that elastomers are nearly incompressible. Consequently, they are characterized by ν approaching 0.5 and high values of K/G (where ν, K and G represent the initial Poisson's ratio, bulk modulus colorred and bulk modulus, respectively). The classical buckling pressure of elastic thin spherical shells is given by (3)

$$\Delta P_{cr}^{up} = \frac{2E}{\sqrt{3(1-\nu^2)}}\eta^2. \tag{S13}$$

By introducing

$$E = \frac{9KG}{3K+G} \text{ and } \nu = \frac{3K-2G}{2(3K+G)} \tag{S14}$$

Eq. (S13) can be rewritten in terms of K/G as

$$\frac{\Delta P_{cr}^{up}}{G} = 4\frac{\frac{K}{G}}{\sqrt{\left(\frac{K}{G}\right)^2 + \frac{4}{3}\frac{K}{G}}}\eta^2. \tag{S15}$$

As such, we anticipate that as K becomes larger, the value of ΔP_{cr}^{up} will increase asymptotically. To verify this point, we perform a number of FE simulations on a shell with $\eta = 0.22$ where we systematically vary the normalized bulk modulus K/G from 10^1 to 10^9 (note that $K/G \approx 5 \times 10^3$ for PDMS mixed in a base polymer to curing agent ratio of 10:1 (9) and $K/G \approx 3 \times 10^3$ when the ratio is 5:1 as in our micrometer scale capsules (10)). The results of Fig. S21 show that for $K/G > 1 \times 10^3$ the change in ΔP_{cr}^{up} is less than 0.1 % as the K is varied from 10^3 to 10^9 Further, in Fig. S21B we compare the evolution of ΔP_{cr}^{up} as a function of K as predicted by Eq. (S15) with the data extracted from our FE simulations. Again, we find that the dependence of ΔP_{cr}^{up} on K is weak. Finally, in Fig. S21C we show the evolution of the critical volumes on volume controlled loading and unloading as a function of K and again find a weak dependence. Since approximating the material as incompressible introduces a negligible error (0.7 ‰ assuming $K/G = 1 \times 10^3$ and using Eq. (S15)), we use a perfectly incompressible material model in the simulations.

Scaling laws. We start by noting that analytical formulas are well established to describe the initial behavior of spherical shells subject to uniform external pressure (3, 11, 12). These formulas are derived using thin shell theory and therefore their accuracy is limited for capsules with $\eta \approx 0.3$ such as the microcapsules produced in this work. However, they can be still used to explain the general trends observed in the data.

Critical points:

It is well known that for a thin spherical shell subjected to a pressure loading the difference between the external and internal pressure of the shells and volume at which buckling is triggered is given by (13)

$$\Delta P_{cr}^{up} = \frac{2E}{\sqrt{3(1-\nu^2)}}\left(\frac{t}{R}\right)^2. \tag{S16}$$
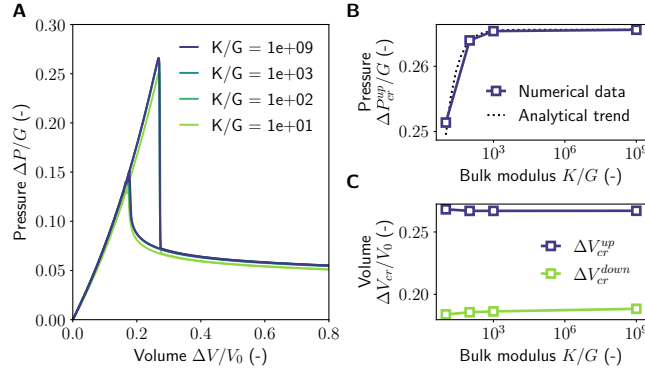
Fig. S21. Influence of the material bulk modulus. A, Simulated pressure-volume characteristics for a shell with $\eta = 0.22$ made out of a Neo-Hookean material for different values of the normalized bulk modulus K/G. **B**, Relation between the normalized bulk modulus K/G and the normalized shell critical pressure $\Delta P_{cr}^{up}/G$. The dashed line represents the analytical scaling law given by Eq. (S15). **C**, Relation between the normalized bulk modulus K/G and the change in volume at which the instabilities on volume-controlled loading (ΔV_{cr}^{up}) and unloading (ΔV_{cr}^{down}) occur for the curves plotted in A.

For an incompressible material with $\nu = 0.5$, $E = 2G(1+\nu) = 3G$ and Eq. (S16) reduces to

$$\Delta P_{cr}^{up} = \frac{6G}{1.5}\eta^2 = 4G\eta^2, \tag{S17}$$

where $\eta = t/R$. Further, the change in internal volume at which buckling is triggered can be expressed as (13)

$$\Delta V_{cr}^{up} = \eta V_0^{mid}, \tag{S18}$$

where $V_0^{mid} = 4\pi R^3/3$ is the initial volume enclosed by the midsurface of the shell. Using Eq. (S6), V_0^{mid} can be rewritten as

$$V_0^{mid} = \frac{V_0}{(1-\eta/2)^3}, \tag{S19}$$

where $V_0 = 4\pi R_i^3/3$ is initial volume of the gas-filled cavity (R_i denoting the inner radius of the shell). Taking a Taylor series, Eq. (S19) can be approximated with second order accuracy as

$$V_0^{mid} \approx V_0\left(1 + \frac{3\eta}{2}\right). \tag{S20}$$

Finally, substitution of Eq. (S20) into Eq. (S18) yields

$$\Delta V_{cr}^{up} \approx \eta\left(1 + \frac{3\eta}{2}\right)V_0, \tag{S21}$$

As shown in Figs. S22A and B, Eqs. (S17) and (S21) closely match the numerically obtained values for ΔP_{cr}^{up} and ΔV_{cr}^{up} for small η. For $\eta > 0.15$, the accuracy of the equation becomes limited since the shells can no longer be assumed to be thin, but qualitatively the trends line up well.

Next, we use these formulas to predict the total external pressure at the critical point, P_{cr}^{up}

$$P_{cr}^{up} = \Delta P_{cr}^{up} + P_{int,cr}, \tag{S22}$$

where $P_{int,cr}$ denoted the critical internal pressure caused by the compression of the gas inside the capsule. Using Eq. (S9), $P_{int,cr}$ can be expressed as

$$P_{int,cr} = P_0\left(\frac{1}{1 - \frac{\Delta V_{cr}^{up}}{V0}} - 1\right) = P_0\left(\frac{1}{1 - \eta(1 + 3\eta/2)} - 1\right), \tag{S23}$$

where P_0 is the atmospheric pressure. Substitution of Eqs. (S17) and (S23) into Eq. (S22) yields

$$\frac{P_{cr}^{up}}{P_0} = 4\frac{G}{P_0}\eta^2 + \frac{1}{1 - \eta(1 + 3\eta/2)} - 1. \tag{S24}$$

In Fig. S22C we compare the predictions of this equation to numerically obtained data and find that it accurately predicts the trend, especially for low values of η.

Change in volume upon collapse: Next, we derive a scaling law for the change in volume of the capsule as it suddenly collapses at P_{cr}^{up} when under pressure controlled conditions, ΔV_{plat}^{up}. Note that ΔV_{plat}^{up} is proportional to the width of the plateau in the pressure-volume characteristic of a metafluid consisting out of many identical capsules under both pressure and volume control conditions (see Section S3.2).
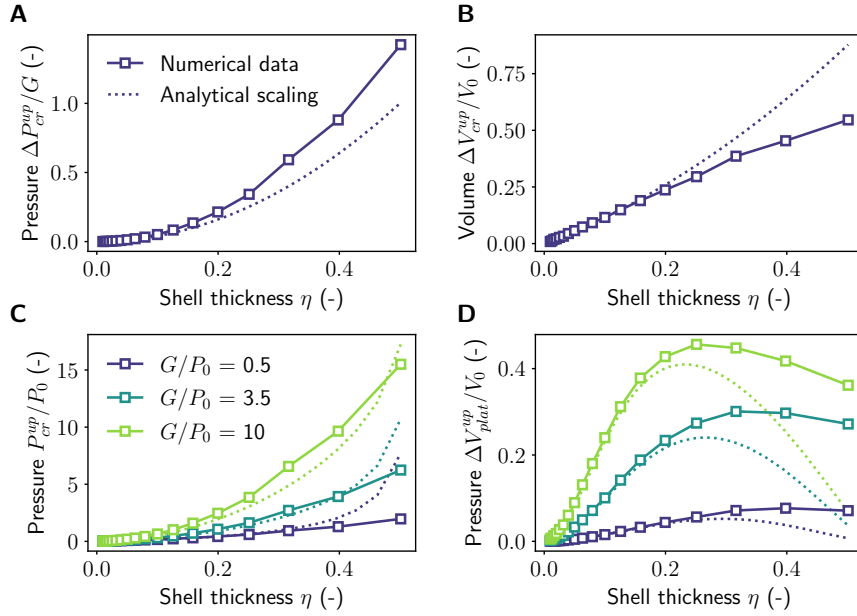
Fig. S22. Scaling of critical pressures and volumes with shell thickness and modulus. A, Evolution of the differential shell pressure at the critical point on loading ΔP_{cr}^{up} in function of the dimensionless shell thickness η. Square markers indicate data points obtained with the FE model while the dotted line corresponds to Eq. (S16). **B**, Evolution of the volume at the critical point upon loading, ΔV_{cr}^{up}, as function of η. The dotted line corresponds to Eq. (S20). **C**, Evolution of the total pressure at the critical point upon loading, P_{cr}^{up}, as a function of η for different values of the dimensionless shear modulus G/P_0. The square markers correspond to numerical FE results and the dotted lines to Eq. (S24). **D**, Evolution of the change in volume during the instability on pressure-controlled loading, ΔV_{plat}^{up}, as function of η for different values of G/P_0. The square markers correspond to FE resutls and the dotted lines correspond to results from Eq. (S27). The line colors correspond to the same values of G/P_0 as indicated in the legend of panel C.

We start by noting that

$$\Delta V_{plat}^{up} = \Delta V_{cr,col}^{up} - \Delta V_{cr}^{up}, \tag{S25}$$

where $\Delta V_{cr,col}^{up}$ is the volume of the collapsed capsule after the instability and ΔV_{cr}^{up} is given by Eq. (S21). After collapse the capsule is highly deformed and its behavior is no longer captured accurately by analytical models. However, our FE simulations show that in the collapsed state $\Delta P_{shell}(\Delta V_{cr,col}^{up}) \ll P_{int}(\Delta V_{cr,col}^{up})$, so that the influence of the shell stiffness can be neglected. As such, $\Delta V_{cr,col}^{up}$ can be estimated from Eq. (S9) as:

$$\frac{\Delta V_{cr,col}^{up}}{V_0} = 1 - \frac{1}{\frac{P_{cr}^{up}}{P_0} + 1} \tag{S26}$$

Substitution of Eq. (S24) into Eq. (S26) yields

$$\frac{\Delta V_{plat}^{up}}{V_0} = 1 - \frac{1}{4\frac{G}{P_0}\eta^2 + \frac{1}{1-\eta(1+3\eta/2)}} - \eta\left(1 + \frac{3}{2}\eta\right). \tag{S27}$$

Eq. (S27) predicts that $\Delta V_{plat}^{up}/V_0$ reaches a maximum for intermediate values of η. This trend is confirmed by the numerical data shown in Fig. S22D. However, Eq. (S27) starts to largely underestimate the numerical data for η past this maximum largely due to the overestimation of ΔV_{cr}^{up}.

Influence of shear flow. When a metafluid flows, every point in the fluid experiences a shear stress τ_{ext} proportional to the viscosity of the fluid, η_0, and the spatial velocity gradient. If this shear load is sufficiently large, the relation between the hydrostatic pressure applied to a capsule and the resulting volume is modified. The reason is that the shear load deforms the sphere approximately into an oblate ellipsoid with the major axis rotated at 45° to the flow lines and that such a shape has a lower buckling pressure than a sphere (14). The change in shape of the capsule due to a simple shear stress τ_{ext} can be estimated analytically for a thin spherical shell made of an incompressible material and surrounded by an incompressible fluid (15). According to this model, the Taylor parameter D is given by

$$D = \frac{L-B}{L+B} = \frac{25}{12}\frac{\tau_{ext}}{G\eta_0}, \tag{S28}$$

where L and B are the major and minor radii of the ellipsoid, respectively. Since it has been shown that the critical buckling pressure ΔP_{cr}^{up} of oblate ellipsoids scales with the square of their aspect ratio B/L (16), it follows that

$$\frac{\Delta P_{cr}^{up}}{G} \propto \left(\frac{1 - \dfrac{25}{12}\dfrac{\tau_{ext}}{G\eta_0}}{1 + \dfrac{25}{12}\dfrac{\tau_{ext}}{G\eta_0}} \right)^2 .$$ [S29]
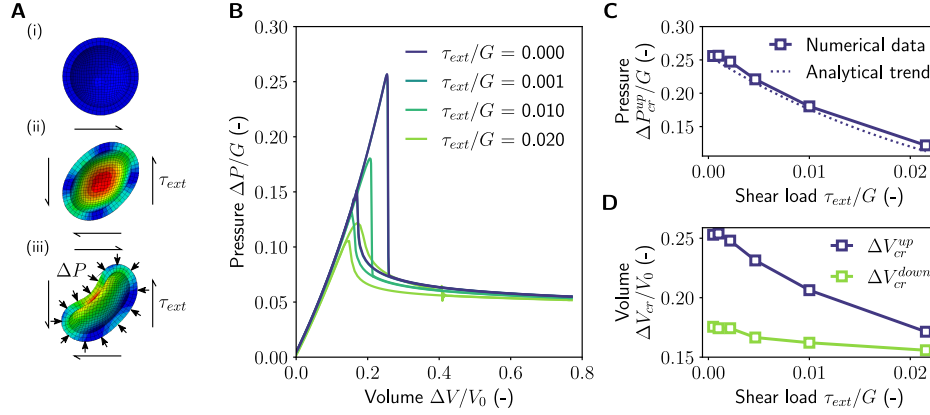
Fig. S23. Influence of a shear load on the pressure-volume characteristic. A, Illustration of the simulation procedure: (i) initial spherical shape of the capsule, (ii) a shear load τ_{ext} is applied on the outer surface, (iii) a uniform normal pressure ΔP is applied on top of τ_{ext}. **B**, Simulated pressure-volume characteristics for a shell with $\eta = 0.22$ subjected to a constant external shear load τ_{ext}. **C**, Relation between the normalized shear load τ_{ext}/G and the critical shell pressure $\Delta P_{cr}^{up}/G$ for a spherical capsule with $\eta = 0.22$. The dashed line represents the analytical scaling law provided by Eq. (S29). **D**, Relation between the normalized shear load τ_{ext}/G and the change in volume at which the instabilities under volume-controlled conditions are triggered upon loading (ΔV_{cr}^{up}) and unloading (ΔV_{cr}^{down}).

To validate the predictions of Eq. (S29), we perform a series of FE simulations in which we apply to the outer surface of the models a distributed load consistent with a uniform shear stress in the surrounding medium τ_{ext} prior to loading the capsule hydrostatically (Fig. S23A). Note that the models used for these simulations comprise three dimensional elements rather than axisymmetric ones. In Fig. Fig. S23B we report results for a spherical capsule with $\eta = 0.22$. These results indicate that Eq. (S29) accurately captures the drop in ΔP_{cr}^{up} as τ_{ext}/G is increased (Fig. S23C). They also show that the critical volumes on loading ΔV_{cr}^{up} follows a similar trend, while ΔV_{cr}^{down} is less sensitive to the shear load (Fig. S23D).

For $\eta = 0.3$ and $G = 400\,\text{kPa}$, which are typical values for the produced microcapsules, the total critical pressures P_{cr}^{up} and P_{cr}^{down} change by less than 2 % if τ_{ext} remains below 620 Pa. Below this limit, these capsules can be considered to be unaffected by the flow field such that all modeling techniques presented in this paper for individual capsules and metafluids yield accurate results even though they assume hydrostatic loading.

S3.2. Modeling interactions between capsules.

S3.2.1. Systems with finite number of capsules. In our experiments we impose a change in the volume of the metafluid ΔV and measure the resulting pressure in the metafluid P_{ext}. As such, the change in volume of the i-th capsule in the pressurized state, $\Delta V^{(i)}$, is subjected to the constraint

$$\Delta V = \sum_{i=1}^{N} \Delta V^{(i)},$$ [S30]

since we assume that the fluid is incompressible. Further, we assume that all spherical capsules in the fluid are subjected approximately to the same pressure P_{ext},

$$P_{ext} = P_{ext}^{(1)}\left(\Delta V^{(1)}\right) = P_{ext}^{(2)}\left(\Delta V^{(2)}\right) = ... = P_{ext}^{(N)}\left(\Delta V^{(N)}\right),$$ [S31]

where $P_{ext}^{(i)}$ denotes the pressure to which the i-th capsule is subjected. Note that this assumption is valid if the piston is small enough such that pressure fluctuations propagate quickly throughout the entire fluid and the hydrostatic pressure difference over the height of the fluid is small compared to the typical pressure in the system. With an upper estimate for the density of the fluid at $1000\,\text{kg/m}^3$, the hydrostatic pressure drop for a container with a height of 30 cm is approximately 3 kPa. A lower estimate for the speed of sound in the fluid is the speed of sound in air which is approximately 330 m/s. For a container with as typical size 30 cm, this means that dynamic pressure differences throughout the fluid remain below 3 kPa as long as the speed with which the pressure changes is below 3300 kPa/s.

Since in our system the pressure is approximately equal for all components in the system and the volumes add up to produce the global ΔV, the capsules and the fluidic medium are said to be loaded in series. This means that the pressure-volume

characteristic of a system can be obtained by evaluating the pressure-volume characteristics of the different constituents at a given pressure and adding up all the resulting volumes. Operationally, to determine all of the equilibrium configurations of a metafluid comprising N capsules, we first find for each capsule all stable volumes that result in a predefined set of pressure values. Then, for each value of pressure, we determine the equilibrium states by making all possible combinations of those volumes. As shown in Fig. S24A, for a suspension comprising N identical capsules through this process we identify $N + 1$ equilibrium branches. When the suspension is loaded by controlling ΔV, the first branch is initially followed until the critical buckling pressure of the capsules, P_{cr}^{up}, is reached. At that point, a capsule snaps and the pressure drops (at constant ΔV) until it reaches the next branch. This process then repeats until all N capsules are collapsed, leading to a saw-tooth pattern with N peaks at P_{cr}^{up}. Note that if ΔV is divided by N, the branch for which all capsules are in the spherical configuration as well as that for which all capsules are in the collapsed configuration collapse on each other for all N (Fig. S24B) The other $N - 1$ branches are uniformly interpolated between these two branches (17).
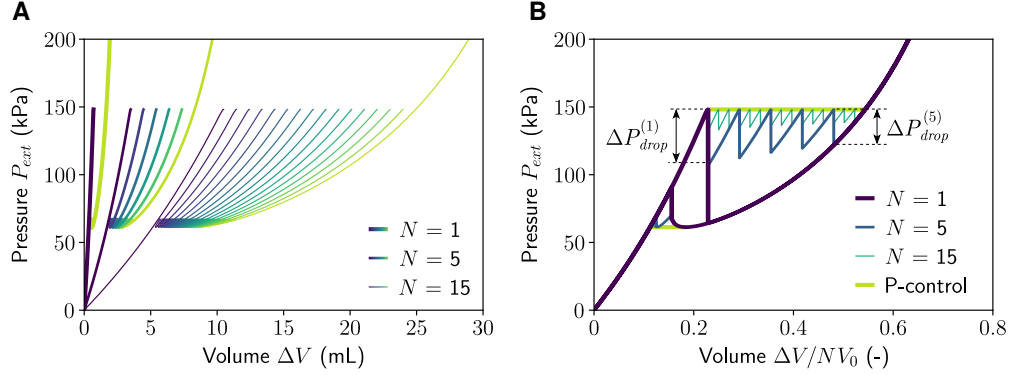
Fig. S24. Interaction between many identical spherical capsules. A, Quasi-static pressure-volume characteristics for a system of $N = 1$, 5 and 15 identical spherical capsules ($R = 10$ mm, $t = 2$ mm, $G = 600$ kPa) suspended in an incompressible medium. The color of the branches indicates the ratio of capsules in the collapsed configuration. **B**, Dynamic pressure-volume characteristics of the same systems under volume controlled inflation and deflation. The volume axis is normalized by the total initial internal volume of the capsules NV_0 such that the fully spherical and fully collapsed branches are coincide for all N. As indicated on the figure for the system with $N = 5$, $\Delta P_{drop}^{(n)}$ is the drop in pressure caused by the collapse of the n-th capsule. As N increases, the pressure drop for every capsule in the system decreases and the characteristics for volume control converge to the pressure control case.

Next, we investigate the effect of N on the magnitude of the pressure drops in the saw-tooth pattern. To this end, we note that, when the n-th capsule starts to collapse,

$$P_{ext} = P_{cr}^{up}, \qquad [S32]$$

and the corresponding ΔV is given by Eq. (S30). Since all capsules are identical, at this point their change in volume is $\Delta V_{cr,col}^{up}$ for the $n - 1$ capsules that are already collapsed and $\Delta V_{cr,sph}^{up}$ for the other $N - (n - 1)$ capsules (including the capsule that is about to collapse) that are in the spherical state (Fig. S25A). It follows that the total change in volume of the capsules when the n-th capsule starts to collapse, $\Delta V_{drop}^{start,(n)}$, is given by

$$\Delta V_{drop}^{start,(n)} = (N - n + 1)\Delta V_{cr,sph}^{up} + (n - 1)\Delta V_{cr,col}^{up}. \qquad [S33]$$

Since the volume is controlled during the tests, the change in volume of the capsules after the collapse of the n-th capsule has ended, $\Delta V_{drop}^{end,(n)}$, is identical to $\Delta V_{drop}^{start,(n)}$,

$$\Delta V_{drop}^{start,(n)} = \Delta V_{drop}^{end,(n)}. \qquad [S34]$$

Even though the total change in volume of the capsules remains constant, the volume of the individual capsules has changed because of the snapping of the n-th capsule. We estimate this change in volume by approximating the pressure-volume curve of capsules in the spherical and collapsed state with a first order Taylor series around P_{cr}^{up} and express $\Delta V_{drop}^{end,(n)}$ as

$$\Delta V_{drop}^{end,(n)} \approx (N - n)\left(\Delta V_{cr,sph}^{up} - \Delta P_{drop}^{(n)} \left.\frac{d\Delta V}{dP}\right|_{cr,sph}^{up}\right) + n\left(\Delta V_{cr,col}^{up} - \Delta P_{drop}^{(n)} \left.\frac{d\Delta V}{dP}\right|_{cr,col}^{up}\right), \qquad [S35]$$

where $\Delta P_{drop}^{(n)}$ denotes the drop in pressure caused by the collapse of the n-th capsule (Fig. S25A). Substitution of Eqs. (S33) and (S35) into Eq. (S34) yields

$$\Delta P_{drop}^{(n)} \approx \frac{\Delta V_{cr,col}^{up} - \Delta V_{cr,sph}^{up}}{(N - n)\left.\frac{d\Delta V}{dP}\right|_{cr,sph}^{up} + n\left.\frac{d\Delta V}{dP}\right|_{cr,col}^{up}}. \qquad [S36]$$

In this equation, the numerator represents the change in volume of an individual capsule when it collapses at P_{cr}^{up} under pressure controlled conditions. This value only depends on the geometry of the capsules and it does not vary with the number of capsules N. on the other hand, the denominator represents the inverse of the slope near P_{cr}^{up} of the branch of the suspension pressure-volume curve on which n capsules are in the collapsed state. This slope scales with the number of capsules N, so

$\Delta P_{drop}^{(n)}$ decreases as N increases (i.e. $\Delta P_{drop}^{(n)} \propto N^{-1}$). We also note that, since the derivatives of ΔV_{sph} and ΔV_{col} are generally not identical, ΔP_{drop}^n is different for every capsule (i.e. it varies with n) (17, 18). In particular, for the first and last capsule to collapse, ΔP_{drop} is given by

$$\Delta P_{drop}^{(1)} \approx \frac{\Delta V_{cr,col}^{up} - \Delta V_{cr,sph}^{up}}{N} \left. \frac{dP_{sph}}{d\Delta V} \right|_{P=P_{cr}^{up}} \quad \text{and} \quad \Delta P_{drop}^{(N)} \approx \frac{\Delta V_{cr,col}^{up} - \Delta V_{cr,sph}^{up}}{N} \left. \frac{dP_{col}}{d\Delta V} \right|_{P=P_{cr}^{up}}, \qquad \text{[S37]}$$

respectively. For all other capsules, ΔP_{drop} lies between these two values which means that ΔP_{drop} varies proportionally with N^{-1} for all capsules. The decreased magnitude of the pressure drops with N is due to the fact that the sudden reduction in volume experienced by a capsule upon snapping can be compensated by a slight expansion of the surrounding $N1$ capsules. To verify this scaling, we numerically evaluate the pressure-volume characteristic of systems with N identical capsules. We then extract from each simulation the N values for $\Delta P_{drop}^{(n)}$ and plot them as points in Fig. S25B. We find that for large values of N all numerical data points lie between the approximate bounds provided by Eq. (S37), confirming the scaling of ΔP_{drop} with N^{-1}. Finally, Eq. (S36) also shows that, for large N, ΔP_{drop} tends to zero, so that the saw-tooth pattern converges to a horizontal plateau at the pressure P_{cr}^{up} for loading.
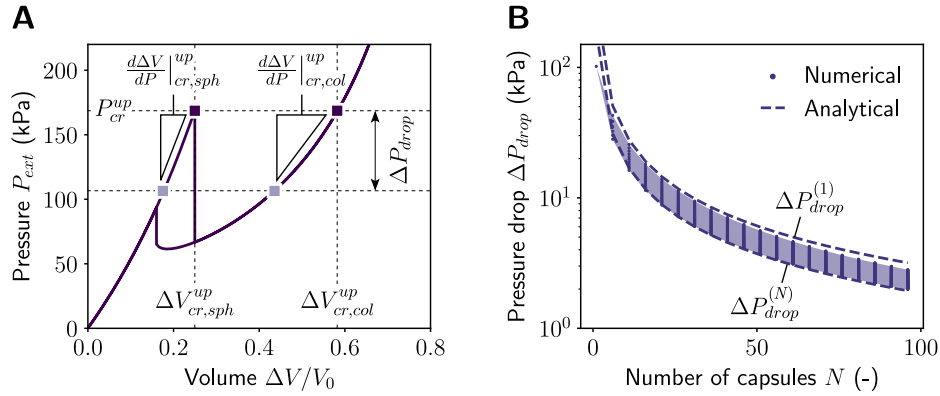
Fig. S25. Scaling of the pressure drop with the number of capsules. A, Pressure-volume curve for a spherical capsules with $R = 10\,\text{mm}$, $t = 2\,\text{mm}$ and $G = 600\,\text{kPa}$) upon inflation and deflation. **B**, Drop in pressure caused by the collapse of a capsule ΔP_{drop} as a function of the number of capsules fluid with N for a suspension of shells all identical to that considered in c A. Dots denote ΔP_{drop} recorded in numerical simulations upon collapse of each capsule. The colored area is their envelope. Dashed lines correspond to the analytical approximations for ΔP_{drop} of the first and last capsule to collapse (Eq. (S37)).

S3.3. Ray tracing simulations. We performed 3D ray tracing simulations using the geometric optics module in COMSOL v6.1.

Individual capsules. We started by focusing on two individual capsules:

- a capsule in its initial spherical state whose geometry was generated using basic geometry tool in COMSOL;

- a capsule in its collapse state. Note that collapsed shape is extracted from our FE simulations. More specifically, we used the shape of the inner cavity of the capsule, since we assume that the PDMS shell and the PDMS oil have a close refractive index and that any effect would be dominated by the contrast in refractive index between the PDMS oil and the air which are $n_{PDMS} \approx 1.5$ and $n_{air} \approx 1$. We neglected any change that might occur to the refractive index of the air under variable pressure conditions.

In our simulations rays arranged on a hexapolar pattern with a power of 1 W and a radius of $R_{beam} = 95\mu m$ are initiated $500\mu m$ away from the capsules. The analysis is stopped when the rays have travelled for 5 mm, taking into account reflections on the surface of the capsules. As shown in Fig. 4A of the main text, we find that spherical and collapsed capsules exhibit distinct scattering behaviors when interacting with incident rays. To check for the robustness of these results, we conducted simulations for different orientations of the incoming rays. Snapshots extracted from these simulations are shown in Fig. S26.

Further, we systematically quantified both the transmittance and focusing efficiency for incident angles $\theta \in [0, 180]$ (Fig. S27A). To measure the transmittance, we placed a power sensor at the focal length of the capsule, f (estimated from measurements of the spot diagram) for angles $\theta <= 90$ and at a distance $-f$ for $\theta > 90$ (to make sure to measure transmitted rays). The transmittance T was then obtained by integrating the power density recorded on the power sensor and dividing it by the power of the incident ray (fixed at 1 W),

$$T = \frac{Power_{transmitted}}{Power_{incident}}. \qquad \text{[S38]}$$

To obtain the focusing efficiency, we integrated the power density recorded on the portion of the power sensor where it is above the half maximum, $Power_{FWHM}$, and divided it by the transmitted power (19, 20)

$$F = \frac{Power_{FWHM}}{Power_{transmitted}}. \qquad \text{[S39]}$$
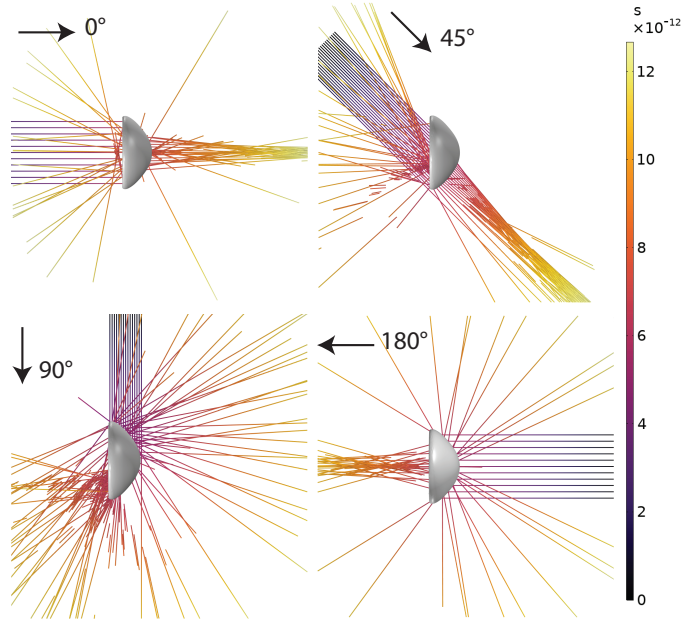
Fig. S26. Ray tracing simulations. Results for different orientation of the incident rays. Color map corresponds to time during ray propagation.

As shown in Fig. S27B, we find that the average transmittance over all angles is ≈70%, with a maximum of 99% for $\theta = 180°$(concave side facing the incident rays). We also find that the average focusing efficiency is above 40% for a wide range of angles, with a maximum of ≈60% for $\theta = 20°$.
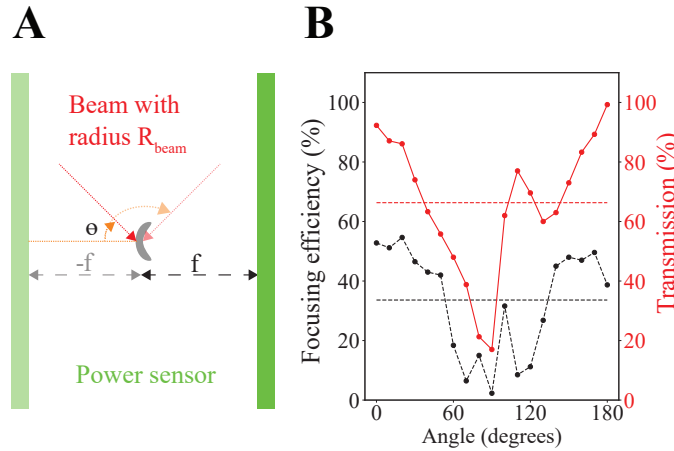

Fig. S27. Effect of incident angle. A Schematics of the simulations. **B** Transmittance and focusing efficiency as function of the incident angle θ. Dashed lines denote the average values across all angles.

Array of capsules. We also considered a dense cluster of capsules (with outer radius $R_o = 250\mu m$) arranged on a 8×8×8 FCC lattice with a volume fraction of 0.6 (resulting to a center-to-center distance of $2.06R_o$ between neighboring spheres). We explored three scenarios: (1) an array of spherical capsules, (2) an array of randomly oriented collapsed capsules all with the convex side facing the rays, and (3) an array of randomly oriented collapsed capsules. Note that we chose all collapsed capsules to have the same projected area as the spherical ones. In the simulations rays arranged on a hexapolar pattern with a power of 1 W and a radius $R_{beam} = 500\mu m$ are initiated 5 mm away from the array of capsules. To quantify this light scattering behavior of the three considered arrays of capsules, we monitored the light reflected onto a square screen with an edge length of 15 mm positioned at a distance of 15 mm from the arrays (Fig. S28A).

In Fig. S28B we show the power density collected on the screen for the three considered arrays of capsules. We find that the transmitted power is much larger for the two arrays of collapsed capsules. Furthermore, we observe that the randomly oriented array of collapsed particles proves more effective in light transmission. To quantify this effect, we calculate the transmission, T, as defined in Eq. (S38). The results reported in Figure S28C show that the transmission for the array of ordered collapsed capsules is ≈100 % larger that that of the array of spherical microcapsules - an increase that can be attributed to the lensing

capability of the collapsed particles. Finally, when we compare the arrays of collapsed ordered and randomly oriented capsules, we find that the transmission is ≈60 % higher for the latter. Such increase can be attributed to the decreased projected area of the randomly oriented capsules in the plane perpendicular to the incoming rays. Indeed when we measure the coverage area for the arrays of ordered and randomly oriented collapsed capsules, we find that the latter is reduced by 58 %. This decrease in coverage area is clearly visible in Fig. S28D, where we show cross sections of the three considered arrays. The snapshots clearly indicate that the light rays can penetrate more deeeply the array of randomly oriented collapsed capsules without being deviated by the shells. As such, these results suggest that the experimentally observed tunable optical behavior of our metafluid can be ascribed to a combination of the lensing effect (Fig. S27) and the reduced capsule coverage area within the randomly oriented array of collapsed capsules (Fig. S28D).
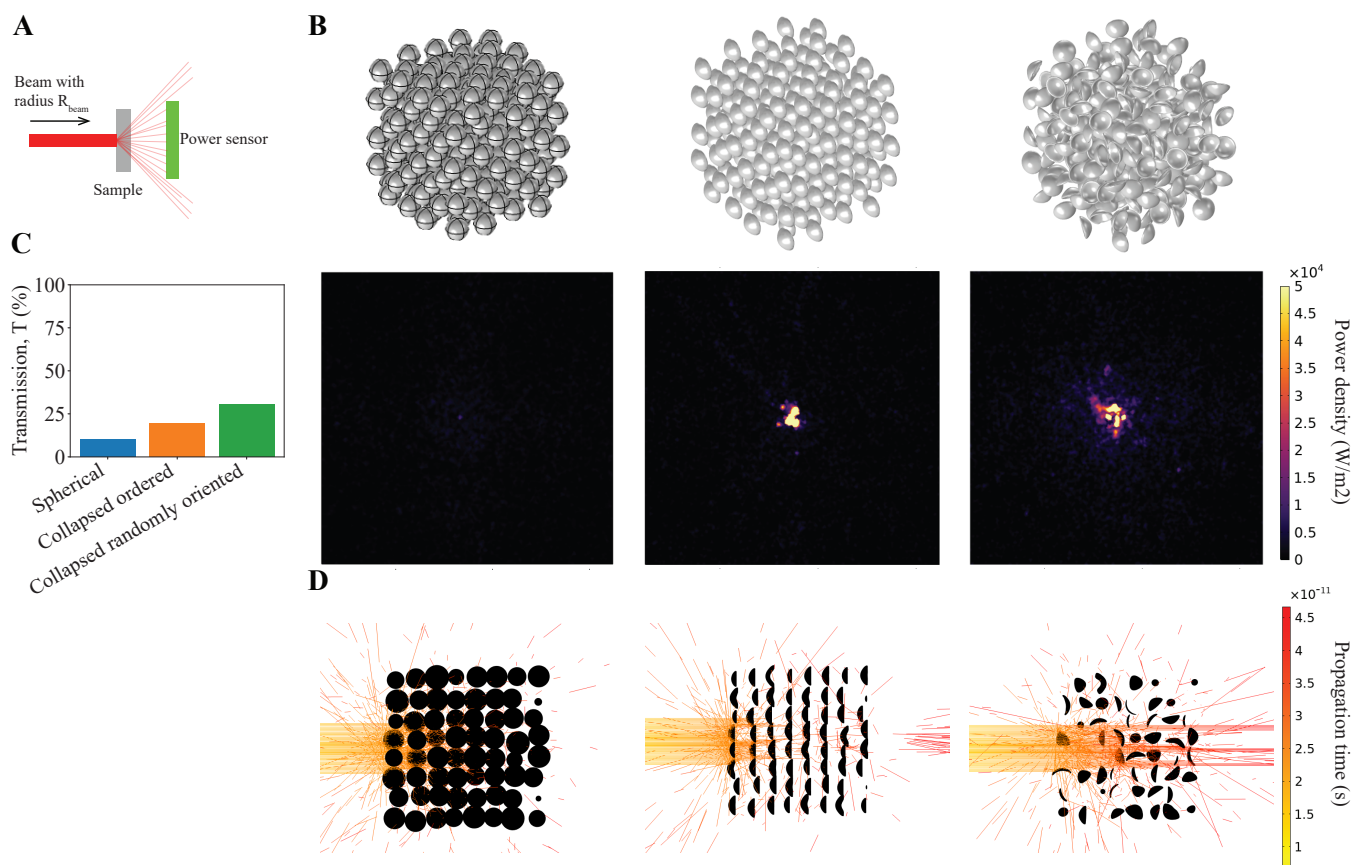
Fig. S28. Ray tracing simulations for a cluster of capsules. A Schematics of the simulation setup. **B** Heat map plots of the transmitted power density in the three different scenarios considered: cluster of spheres (left), cluster of collapsed capsules with their convex side facing the incident beam (middle) and cluster of randomly oriented collapsed capsules (right). **C** Transmitted power measured for the three different scenarios divided by the input power. **D** Numerical snapshots showing the propagation of the light rays across the three considered arrays.

Video S1. Pressure-volume curve of a single capsule. *Centimeter-scale capsule*: To characterize the pressure-volume characteristics of a single centimeter-scale capsule, we place it in a glass container. We then load the system by introducing a volume ΔV of water via a syringe pump and measure the pressure inside the container with a differential pressure sensor. *Micrometer-scale capsule*: To measure the pressure-volume curve of a single micrometer-scale capsule, we place it in a micro-liter glass syringe with immersion oil. In our experiments, the volume inside the syringe is controlled by mechanically connecting the syringe's plunger to a high precision linear stage. To measure the pressure P_{ext}, we inject an air bubble into the syringe and monitor the evolution of its volume when the syringe's plunger moves. *Finite Element simulations*: To model the behavior of single capsules under hydrostatic pressure loading, we conduct a finite element (FE) simulation in Abaqus (Abaqus/CAE 2020, Dassault Systèmes) and then account for the contribution of the compressible gas inside the capsule.

Video S2. Pressure-volume curve of the metafluid. *Metafluid with centimeter-scale capsules*: To characterize the pressure-volume characteristics of a metafluid with centimeter-scale capsules, we place it in a glass container. We then load the system by introducing a volume ΔV of water via a syringe pump and measure the pressure inside the container with a differential pressure sensor. *Metafluid with micro-scale capsules*: To measure the pressure-volume curve of the metafluid with micrometer-scale capsule, we place it in a syringe. The syringe's plunger is slowly displaced to reduce the enclosed volume by ΔV, while keeping the tip closed and monitoring pressure with a pressure sensor.

Video S3. Smart gripper. We exploit the snapping-induced pressure plateau to realize a gripper that can grasp a glass bottle, an egg and a blueberry upon application of the same input. When using water or air as fluid to actuate the jaw, no Δ can be identified that allows us to successfully grasp all three objects. By contrast, when using a metafluid, we can successfully grasp all three objects by injecting $\Delta V = 6.7$ ml.

Video S4. Interactions with flexible structures. We inflate a flexible tube. Upon inflation with glycerol the ballooning instability is triggered for $\Delta V \approx 0.53$ ml. The compliance and pressure plateau of the metafluid offset the instability to $\Delta V \approx = 0.94$ ml.

Video S5. Tunable optical properties. A Harvard logo displayed below the metafluid becomes much clearer for $P_{ext} > P_{cr}^{up}$.

Video S6. Pressure-driven flow. We investigate the flow of a microsuspension in a elliptical channel where we fix the difference of pressure between the inlet and outlet at $\Delta P = P_{in}P_{out} = 50$ kPa. For $P_{in} = 50$ kPa (top) the capsules are all spherical and the flow is much faster than for $P_{in} = 350$ kPa (bottom).

References

1. A. S. Utada, E. Lorenceau, D. R. Link, P. D. Kaplan, H. A. Stone, and D. A. Weitz. Monodisperse double emulsions generated from a microcapillary device. *Science*, 308(5721):537–541, 2005. . URL https://www.science.org/doi/abs/10.1126/science.1109164.

2. *Abaqus/CAE User's Guide (6.14)*, chapter 11.4.3 Part size. Dassault Systèmes, 2014. URL http://130.149.89.49:2080/v6.14/books/usi/default.htm?startat=pt03ch11s04s03.html.

3. John W Hutchinson. Buckling of spherical shells revisited. *Proceedings of the Royal Society A: Mathematical, Physical and Engineering Sciences*, 472(2195):20160577, 2016.

4. Sebastian Knoche and Jan Kierfeld. Secondary polygonal instability of buckled spherical shells. *Europhysics Letters*, 106 (2):24004, apr 2014. . URL https://dx.doi.org/10.1209/0295-5075/106/24004.

5. *Abaqus Theory Guide (6.14)*, chapter 3.6.2 Axisymmetric Shell Elements. Dassault Systèmes, 2014. URL http://130.149.89.49:2080/v6.14/books/stm/default.htm?startat=ch03s06ath80.html.

6. C. Quilliet, C. Zoldesi, C. Riera, A. van Blaaderen, and A. Imhof. Anisotropic colloids through non-trivial buckling. *The European Physical Journal E*, 27:13–20, 2008. ISSN 1292-895X. . URL https://doi.org/10.1140/epje/i2007-10365-2.

7. D.M. Haughton and R.W. Ogden. On the incremental equations in non-linear elasticity — ii. bifurcation of pressurized spherical shells. *Journal of the Mechanics and Physics of Solids*, 26(2):111–138, 1978. ISSN 0022-5096. . URL https://www.sciencedirect.com/science/article/pii/0022509678900170.

8. E. Riks. An incremental approach to the solution of snapping and buckling problems. *International Journal of Solids and Structures*, 15(7):529–551, 1979. ISSN 0020-7683. . URL https://www.sciencedirect.com/science/article/pii/0020768379900817.

9. Ian D Johnston, Daniel K McCluskey, Christabel KL Tan, and Monica C Tracey. Mechanical characterization of bulk sylgard 184 for microfluidics and microengineering. *Journal of Micromechanics and Microengineering*, 24(3):035017, 2014.

10. Tae Kyung Kim, Jeong Koo Kim, and Ok Chan Jeong. Measurement of nonlinear mechanical properties of pdms elastomer. *Microelectronic Engineering*, 88(8):1982–1985, 2011. ISSN 0167-9317. . URL https://www.sciencedirect.com/science/article/pii/S0167931710005964. Proceedings of the 36th International Conference on Micro- and Nano-Engineering (MNE).

11. JMT Thompson. The rotationally-symmetric branching behaviour of a complete spherical shell. *Proceedings of the Koninklijke Nederlandse Akademie van Wetenschappen*, pages 295–311, 1964.

12. Sebastian Knoche and Jan Kierfeld. Buckling of spherical capsules. *Phys. Rev. E*, 84:046608, Oct 2011. . URL https://link.aps.org/doi/10.1103/PhysRevE.84.046608.

13. John W. Hutchinson and J. Michael T. Thompson. Nonlinear Buckling Interaction for Spherical Shells Subject to Pressure and Probing Forces. *Journal of Applied Mechanics*, 84(6), 04 2017. ISSN 0021-8936. . URL https://doi.org/10.1115/1.4036355. 061001.

14. Dominique Barthes-Biesel. Motion and deformation of elastic capsules and vesicles in flow. *Annual Review of fluid mechanics*, 48:25–52, 2016.

15. D Barthès-Biesel, JM Rallison, D Barthès-Biesel, and JM Rallison. The time-dependent deformation of a capsule freely suspended in a linear shear flow. *Journal of Fluid Mechanics*, 113:251–267, 1981.

16. K.M. Mushtari and K.Z. Galimov. *Non-linear Theory of Thin Elastic Shells*, chapter 13, pages 310–311. NASA TT F-. National Science Foundation, 1957. ISBN 9780608310121. URL https://archive.org/details/nasa_techdoc_19980231031/mode/2up.

17. Itamar Benichou and Sefi Givli. Structures undergoing discrete phase transformation. *Journal of the Mechanics and Physics of Solids*, 61(1):94–113, 2013. ISSN 0022-5096. . URL https://www.sciencedirect.com/science/article/pii/S0022509612001883.

18. G. Puglisi and L. Truskinovsky. Mechanics of a discrete chain with bi-stable elements. *Journal of the Mechanics and Physics of Solids*, 48(1):1–27, 2000. ISSN 0022-5096. . URL https://www.sciencedirect.com/science/article/pii/S002250969900006X.

19. Marcus Ossiander, Maryna Leonidivna Meretska, Hana Kristin Hampel, Soon Wei Daniel Lim, Nico Knefz, Thomas Jauk, Federico Capasso, and Martin Schultze. Extreme ultraviolet metalens by vacuum guiding. *Science*, 380(6640):59–63, 2023. . URL https://www.science.org/doi/abs/10.1126/science.adg6881.

20. Mohammadreza Khorasaninejad, Wei Ting Chen, Robert C. Devlin, Jaewon Oh, Alexander Y. Zhu, and Federico Capasso. Metalenses at visible wavelengths: Diffraction-limited focusing and subwavelength resolution imaging. *Science*, 352(6290): 1190–1194, 2016. . URL https://www.science.org/doi/abs/10.1126/science.aaf6644.